Astronomy & Astrophysics manuscript no. sn2011dh-2-no-hydro-v5
April 4, 2014

The type IIb SN 2011dh - 2 years of observations and modelling of the bolometric and photometric lightcurves.

M. Ergon[1], A. Jerkstrand[2] **Group 1 (in alphabetic order):**, M. Bersten[6], N. Elias-Rosa[5], C. Fransson[1], M. Fraser[2], A. Pastorello[3], J. Sollerman[1], S. Taubenberger[4], S. Valenti[7,8] **Group 2 (in alphabetic order, to be extended):**, S. Benetti[3], S. Smartt[2], and L. Tomasella[3]

[1] The Oskar Klein Centre, Department of Astronomy, AlbaNova, Stockholm University, 106 91 Stockholm, Sweden
[2] Astrophysics Research Center, School of Mathematics and Physics, Queens University Belfast, Belfast, BT7 1NN, UK
[3] INAF, Osservatorio Astronomico di Padova, vicolo dell'Osservatorio n. 5, 35122 Padua, Italy
[4] Max-Planck-Institut für Astrophysik, Karl-Schwarzschild-Str. 1, D-85741 Garching, Germany
[5] Institut de Ciències de l'Espai (IEEC-CSIC), Facultat de Ciències, Campus UAB, E-08193 Bellaterra, Spain.
[6] Kavli Institute for the Physics and Mathematics of the Universe, Todai Institutes for Advanced Study, University of Tokyo, 5-1-5 Kashiwanoha, Kashiwa, Chiba 277-8583, Japan
[7] Las Cumbres Observatory Global Telescope Network, 6740 Cortona Dr., Suite 102, Goleta, CA 93117, USA
[8] Department of Physics, University of California, Santa Barbara, Broida Hall, Mail Code 9530, Santa Barbara, CA 93106-9530, USA

Submitted to Astronomy and Astrophysics

ABSTRACT

We present optical and near-infrared (NIR) photometry and spectroscopy of the Type IIb supernova (SN) 2011dh spanning 2 years, and modelling of the bolometric and photometric lightcurves. To model the 0-100 days bolometric lightcurves of SNe 2011dh, 1993J and 2008ax, we use the hydrodynamical model grid and the fitting procedure presented in Ergon et al. (2014a), which allows us to determine the errors in the derived quantities. Using this method we find a helium core mass of $3.4^{+0.6}_{-0.3}$ $M_\odot$ for SN 2011dh and similar values for SNe 1993J and 2008ax. Using a bolometric correction determined with steady-state NLTE modelling we extend the temporal coverage of the model grid to 300 days and applied to SN 2011dh we obtain results in good agreement with those based on the 0-100 days bolometric lightcurve. We present 100-500 days bolometric and photometric lightcurves for the Jerkstrand et al. (2014) steady-state NLTE models and discuss the constraints derived from the those on the model parameters. The optimal 12 $M_\odot$ model, presented and found to give a good agreement with observed nebular spectra in Jerkstrand et al. (2014), shows a good agreement with the observed lightcurves, although the evolution in the MIR is only partly reproduced. Time-dependent NLTE modelling shows that after 600 days a steady-state assumption is no longer valid. The radioactive energy deposition in this phase is likely dominated by the positrons emitted in the decay of ^{56}Co but what energy source is dominating the emitted flux is unclear. We find an excess in the MIR developing between 100 and 200 days, during which an increase in the optical tail decline rates is also observed. Steady-state NLTE models with a modest amount of dust (τ = 0.25) added during this period partly reproduce this behaviour. A modest amount of CO first overtone band emission is detected at 89 and 202 days implying a contribution to the Spitzer 4.5 μm band from CO fundamental band emission. Examining the steady-state NLTE models neither complete CO cooling nor absence of CO cooling in the C/O zone well reproduce the observed Spitzer 4.5 μm flux suggesting an intermediate scenario. Estimates of the sizes of the line emitting regions, ranging from ∼3000 km s^{-1} for the oxygen lines to ∼1500 km s^{-1} for the iron lines, suggest partial mixing of the nuclear burning zones, and the sizes of these regions are in all compared cases smaller than for SNe 1993J and 2008ax. The profiles of the [O I] 6300 Å and Mg I] 4571 Å lines show a remarkable similarity, suggesting these lines to be emitted by the same material and to originate from the O/Ne/Mg zone. We use repetitions of small scale fluctuations in the [O I] 6300 Å and [O I] 6364 Å lines to estimate a line ratio close to 3, consistent with optically thin emission, from 200 days and onwards. This paper concludes our extensive observational and modelling work on SN 2011dh presented in a series of papers. The results from hydrodynamical modelling, steady-state NLTE modelling and stellar evolutionary progenitor analysis presented in Maund et al. (2011), Bersten et al. (2012), Jerkstrand et al. (2014) and this paper are all consistent and suggest an initial mass of ∼13 $M_\odot$ for the progenitor. The initial masses of $\lesssim$15 $M_\odot$ found for SNe 2011dh, 1993J and 2008ax, by hydrodynamical modelling and steady-state NLTE modelling in Jerkstrand et al. (2014) and this paper suggest that all of these Type IIb SNe originates from binary systems, as previously established for SN 1993J.

Key words. supernovae: general — supernovae: individual (SN 2011dh) — supernovae: individual (SN 1993J) — supernovae: individual (SN 2008ax) — galaxies: individual (M51)

1. Introduction

Type IIb supernovae (SNe) are observationally characterized by a transition from Type II (with hydrogen lines) at early times to Type Ib (without hydrogen lines but with helium lines) at later times. The physical interpretation is that these SNe arise from stars that have lost most of their hydrogen envelope, either through stellar winds or interaction with a binary companion. Which of these production channels are dominating is still debated but for SN 1993J, the prime example of such an SN, a companion star was detected by direct observations (Maund

et al. 2004). The evolution of this binary system has been successfully modelled (Podsiadlowski et al. 1993; Stancliffe & Eldridge 2009) and it is widely accepted that the companion was responsible for the removal of the hydrogen envelope. Bright, nearby Type IIb SNe as 1993J, 2008ax and the recent 2011dh are essential to improve our understanding of this class. Observations of the progenitor star in pre-explosion images, a search for the companion star when the SN has faded and multi-method modelling of high quality data, all provide important clues to the nature of Type IIb SNe and their progenitor stars.

In this paper we present the extensive optical and near-infrared (NIR) dataset, covering nearly two years, that we have obtained for SN 2011dh. The first 100 days of this dataset have been presented in Ergon et al. (2014b, hereafter E14a). Detailed hydrodynamical modelling of the SN using those data were presented in Bersten et al. (2012, hereafter B12) and steady-state NLTE modelling of nebular spectra in Jerkstrand et al. (2014, hereafter J14). Identification and analysis of the plausible progenitor star was presented in Maund et al. (2011, hereafter M11) and confirmation of the progenitor identification through its disappearance in E14a.

SN 2011dh was discovered on 2011 May 31.893 UT (Griga et al. 2011) in the nearby galaxy M51 at a distance of 7.8 Mpc (E14a). The SN has been extensively monitored from X-ray to radio wavelengths by several teams. Most observations cover the 3-100 days period, but late time data have been published in Tsvetkov et al. (2012), Van Dyk et al. (2013), Sahu et al. (2013), Shivvers et al. (2013) and Helou et al. (2013). As in E14a we focus on the UV to MIR emission. The explosion epoch, the distance to M51 and the interstellar line-of-sight extinction towards the SN used in this paper, are all adopted from E14a.

The nature of the progenitor star has been a key issue since the identification of a yellow supergiant in pre-explosion images, coincident with the SN (M11; Van Dyk et al. 2011). Recent progress in modelling of the SN (B12; J14; Shivvers et al. 2013) and the disappearance of the progenitor candidate (E14a; Van Dyk et al. 2013) strengthens the hypothesis that the progenitor was a yellow supergiant of moderate mass, as was originally proposed in M11. In this paper we present further modelling in support of this hypothesis. As shown in Benvenuto et al. (2013) a binary interaction scenario that reproduces the observed and modelled properties of the yellow supergiant is possible. HST observations that could detect or set useful constraints on the presence of a companion star are scheduled for Cycle 21.

The paper is organized as follows. In Sect. 2 we present the observations and describe the reduction and calibration procedures and in Sect. 3 we present an observational analysis and comparison of the observations to SNe 1993J and 2008ax. In Sect. 4 we model the bolometric and photometric lightcurves and in Sect. 5 we review the results we have obtained for SN 2011dh so far and the implications for our understanding of Type IIb SNe. Finally, we conclude and summarize the paper in Sect. 6.

2. Observations

The observations during the first 100 days have been described in E14a. The reductions and calibration procedures used for the late time data are the same as in E14a and are described in detail in therein, where we also provide a thorough discussion on the accuracy of the photometry. In this section we focus on issues specifically related to the post 100 days data.

2.1. Imaging

The late time data were obtained with the Liverpool Telescope (LT), the Nordic Optical Telescope (NOT), Telescopio Nazionale (TNG), the Calar Alto 3.5m (CA 3.5m) and 2.2m (CA 2.2m) telescopes, the Asiago 67/92cm Schmidt (AS Schmidt) and 1.82m Copernico (AS 1.82m) telescopes, the William Herschel Telescope (WHT), the Albanova Telescope (AT) and the United Kingdom Infrared Telescope (UKIRT). The late time dataset includes 61 epochs of optical imaging and 9 epochs of NIR imaging which, together with the early time observations, gives a total of 146 epochs of optical imaging and 32 epochs of NIR imaging.

2.1.1. Reductions and calibration

Comparison to photometry on template subtracted images shows that the background contamination is negligible before ∼300 days after which we have used photometry on template subtracted images. The accuracy of the late time photometry depends critically on the accuracy of the S-corrections. The late time JC and SDSS photometry were mainly obtained with the NOT but comparisons between S-corrected NOT, LT and CA 2.2m JC and SDSS observations at ∼300 days show differences at the 5 percent level suggesting that this precision is maintained. We note that in this phase S-corrections are absolutely necessary. For example the difference between the NOT and CA 2.2m *I* band observations are almost one magnitude at ∼300 days if these are not applied, mainly because of the strong [Ca II] 7291,7323 Å and Ca II 8498,8542,8662 Å lines. The late time 2MASS photometry was obtained with a number of different telescopes and although the sampling is sparse the shape of the lightcurves suggests that the errors in the S-corrections are modest.

!We probably add a discussion here, or possible a separate section, on the very late time observations and the uncertainties in these.!

2.1.2. Results

The S-corrected optical and NIR magnitudes and their corresponding errors are listed in Tables 4, 5 and 6 and the Spitzer 3.6 and 4.5 μm magnitudes and their corresponding errors in Table 7. For completeness we also include the magnitudes for the first 100 days already published in E14a. All magnitudes, including the SWIFT magnitudes published in E14a, are shown in Fig. 1 which also shows cubic spline fits using 3-5 point knot separation, error weighting and a 5 percent error floor or, when the sampling is sparse, linear interpolations as well as extrapolations assuming a constant colour to adjacent bands. All calculations in Sect. 3, including the construction of the bolometric lightcurve, are based on these spline fits, interpolations and extrapolations. In these calculations the errors in the fitted splines have been estimated as the standard deviation and then propagated.

2.2. Spectroscopy

The late time data were obtained with the NOT, the TNG, the WHT, the CA 2.2m, the Asiago 1.22m Galileo telescope (AS 1.22m), and the Gran Telescopio Canarias (GTC). The late time dataset includes 18 optical spectra obtained at 13 epochs and 2 NIR spectra obtained at 2 epochs which, together with the early time observations, gives a total of 73 optical spectra obtained at 39 epochs and 20 NIR spectra obtained at 12 epochs.

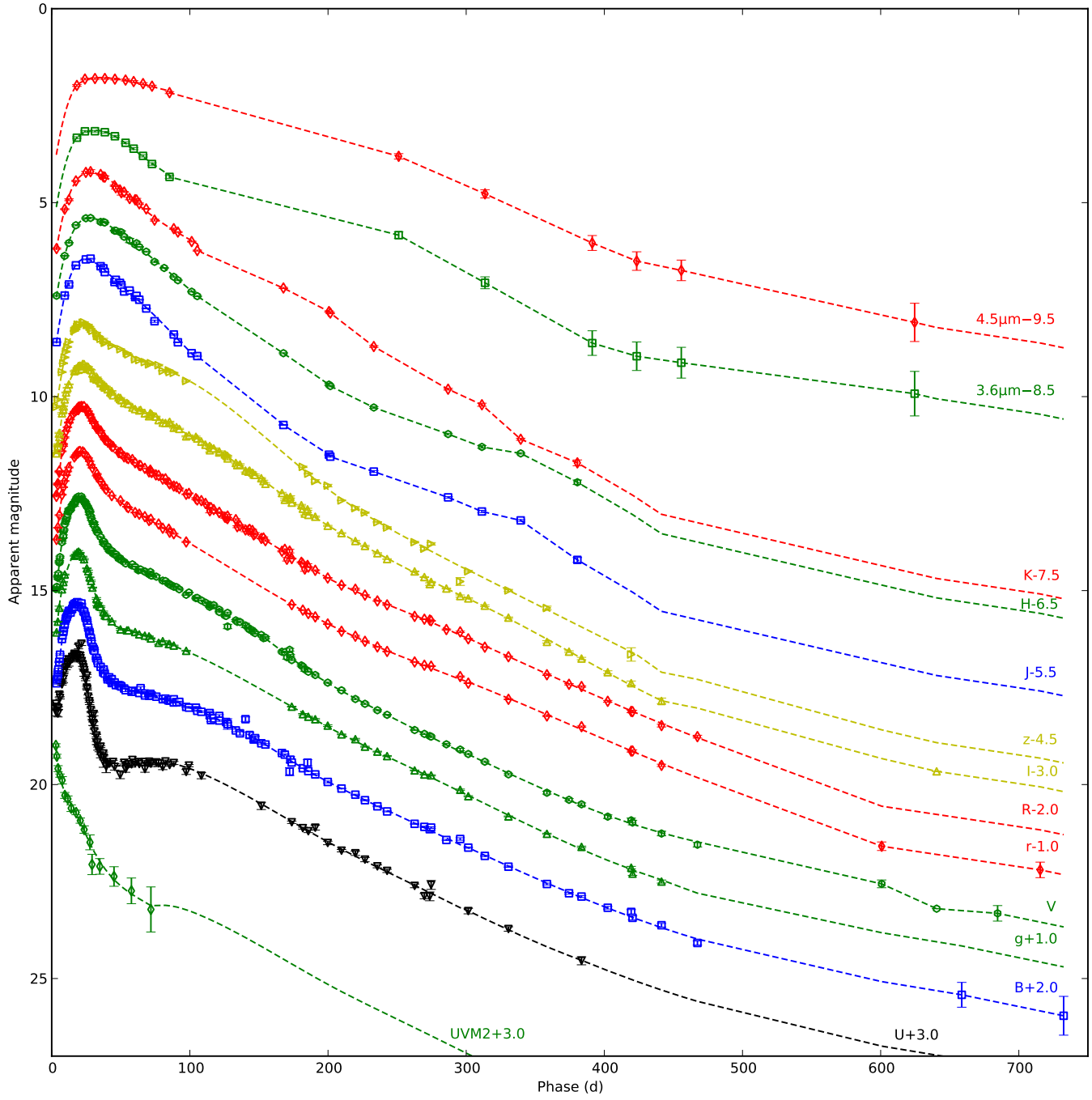

Fig. 1. Photometric evolution of SN 2011dh in the UV, optical, NIR and MIR. For clarity each band has been shifted in magnitude. Each lightcurve has been annotated with the name of the band and the shift applied. We also show combinations of spline fits, interpolations and extrapolations described in Sect 2.1.2 (dashed lines).

2.2.1. Results

All reduced, extracted and calibrated spectra will be made available for download from the Weizmann Interactive Supernova data REPository[1] (WISeREP) (Yaron & Gal-Yam 2012). Figure 3 shows the sequence of observed spectra where those obtained on the same night using the same telescope and instrument have been combined. For clarity some figures in this and the following sections are based on time-interpolations of the spectral sequence as described in E14a. To further visualize the evolution, the spectra have been aligned to a time axis at the right border of the panels. Interpolated spectra were used in the calculations of the bolometric lightcurve (Sect. 3.2) and S-corrections. Figure 2 shows the interpolated optical and NIR spectral evolution of SN 2011dh for 5−425 days with a 20-day sampling. All spectra in this and subsequent figures have been corrected for redshift and interstellar extinction.

[1] http://www.weizmann.ac.il/astrophysics/wiserep/

3. Analysis

In this section we provide an analysis of the data and a comparison of these to the Type IIb SNe 1993J and 2008ax. Besides SN 2011dh, these are the best monitored Type IIb SNe so far. Both occurred in nearby galaxies, have progenitor detections and well constrained explosion epochs. We keep the analysis of the photometric and bolometric evolution observational, as we return to the physical interpretation in Sect. 4, where we present steady-state NLTE and hydrodynamical modelling of these data. The early (0-100 days) evolution of SN 2011dh, as well as comparisons in this phase to SNe 1993J and 2008ax, were discussed in E14a, and here we focus on the evolution after 100 days.

As discussed in E14a, the systematic errors stemming from the uncertainties in distance and extinction are large for all three SNe, which should be kept in mind when absolute quantities are compared. For SNe 1993J and 2008ax we adopt the same values and error bars for the distance and extinction as in E14a. The references for the photometric and spectroscopic data of SNe 1993J and 2008ax used in the comparison are the same as specified in E14a !not true, we use additional late time data!. We note that the lack of S-corrected photometry for SN 1993J complicates the comparison, whereas for SN 2008ax the S-corrected JC photometry by Taubenberger et al. (2011) agrees reasonably well with the JC photometry by Tsvetkov et al. (2009).

3.1. Photometric evolution

Absolute magnitudes were calculated as in E14a. In Fig. 4 we show absolute optical and NIR magnitudes for SN 2011dh as compared to SNe 1993J and 2008ax, and in Table 1 we tabulate the tail decline rates at 100, 200 and 300 days. Most striking is the similarity between the lightcurves, except for a shift towards higher luminosities for SNe 1993J and 2008ax, the shift being larger in bluer bands and negligible in the NIR and most pronounced for SN 2008ax. As discussed in E14a, this difference could be explained by an error in the adopted extinctions.

Given the caveat that SNe 1993J and 2008ax are only partly covered in U and NIR, we find the following general trends. At 100 days the V, R and I decline rates are roughly twice the decay rate of ^{56}Co, and subsequently decrease towards 300 days. The U and B decline rates are significantly lower at 100 days, subsequently approach the other optical decline rates and then evolve similarly. The J and H band decline rates are considerably higher than the optical at 100 days, subsequently approaches those and eventually become considerably lower. For SNe 2011dh and 1993J the K band behaves quite differently than the other NIR bands. At 100 days the decline rate is significantly lower, but as it remains roughly constant, it subsequently approach the other NIR decline rates and eventually becomes considerably higher. As seen in Fig. 1, the optical lightcurves of SN 2011dh flatten considerably after ~450 days, approaching a decline rate similar to, or lower than, the decay rate of ^{56}Co.

Both SNe 2011dh and 1993J were also monitored in the MIR, SN 2011dh in the Spitzer 3.6 and 4.5 μm bands and SN 1993J in the L band, which is similar to the Spitzer 3.6 μm band. For both SNe a strong excess in the MIR develops between ~100 and ~250 days. For SN 1993J the MIR coverage ends at ~250 days and for SN 2011dh the subsequent evolution is fairly similar to the evolution in the optical, and the considerable flattening seen in the optical lightcurves after ~450 days, is also seen in the Spitzer lightcurves.

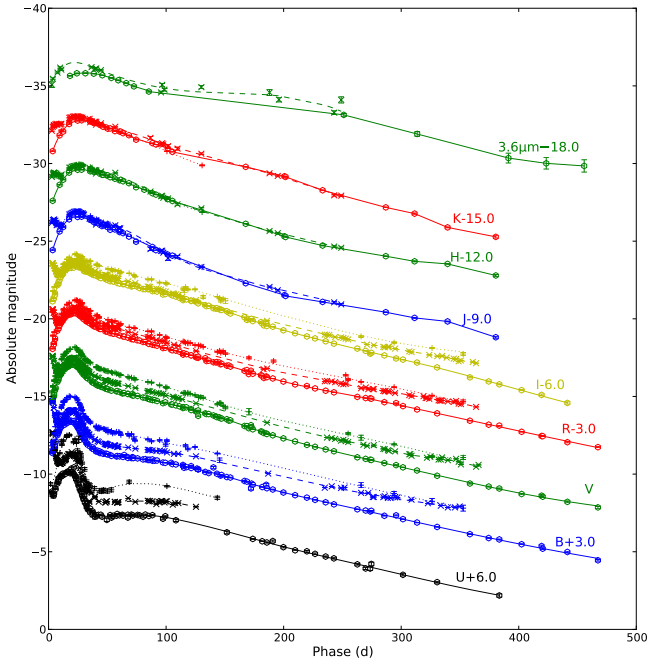

Fig. 4. Photometric evolution of SN 2011dh (dots) in the optical and NIR as compared to SNe 1993J (crosses) and 2008ax (pluses). For clarity each band has been shifted in magnitude. Each lightcurve has been annotated with the name of the band and the shift applied. We also show combinations of spline fits, interpolations and extrapolations described in Sect. 2.1.2 (dashed lines).

!I have removed a discussion on the colour evolution here. Maybe this should be included, I'm not sure. It is a very long paper.!

3.2. Bolometric evolution

As in E14a we have used a combination of the spectroscopic and photometric methods, applied to wavelength regions with and without spectral information respectively, when calculating the pseudo-bolometric lightcurves. The details of these methods have been described in E14a. Combinations of spline fits, interpolations and extrapolations, as decribed in Sect. 2.1.2 and shown in Figs. 1 and 4, have been used to calculate the magnitudes.

Figure 5 shows the U to K (3300-24000 Å) pseudo-bolometric lightcurves for SN 2011dh as compared to SNe 1993J and 2008ax for the 0-500 days period as calculated with the photometric method, and in Table 2 we tabulate the decline rates at 100, 200 and 300 days. Given the caveat that SNe 1993J and 2008ax are not covered in NIR after ~250 and ~150 days respectively, their U to K pseudo-bolometric lightcurves are remarkably similar to the one of SN 2011dh, except for the shift towards higher luminosities discussed previously in Sect. 3.1. The decline rates decrease from ~0.020 mag day^{-1}, roughly twice the decay rate of ^{56}Co, at 100 days to ~0.015 mag day^{-1} at 300 days. There is however a significant increase in the decline rate between ~150 and ~200 days for SN 2011dh, not seen for SNe 1993J and 2008ax. For SN 1993J the decline rate becomes increasingly lower towards 300 days as compared to SNe 2011dh and 2008ax, which is consistent with an increasing contribution from CSM interaction in this phase.

Figure 6 shows the UV to MIR (1900-50000 Å) pseudo-bolometric lightcurve for SN 2011dh, as calculated with the

Table 1. Tail decline rates at 100, 200 and 300 days for SN 2011dh compared to SNe 1993J and 2008ax as measured from cubic spline fits.

SN	Band	Rate (100 d) (mag day^{-1})	Rate (200 d) (mag day^{-1})	Rate (300 d) (mag day^{-1})
2011dh	*U*	0.013	0.019	0.018
2011dh	*B*	0.014	0.019	0.017
2011dh	*V*	0.018	0.021	0.018
2011dh	*R*	0.020	0.019	0.016
2011dh	*I*	0.019	0.021	0.017
2011dh	*J*	0.036	0.017	0.012
2011dh	*H*	0.029	0.019	0.011
2011dh	*K*	0.020	0.020	0.024
1993J	*U*	0.006	...	...
1993J	*B*	0.011	0.017	0.012
1993J	*V*	0.019	0.019	0.017
1993J	*R*	0.022	0.015	0.013
1993J	*I*	0.022	0.019	0.013
1993J	*J*	0.041	0.016	...
1993J	*H*	0.033	0.018	...
1993J	*K*	0.023	0.022	...
2008ax	*U*	0.013	...	...
2008ax	*B*	0.015	0.018	0.016
2008ax	*V*	0.022	0.018	0.017
2008ax	*R*	0.023	0.016	0.015
2008ax	*I*	0.018	0.021	0.013
2008ax	*J*	0.035	...	...
2008ax	*H*	0.032	...	...
2008ax	*K*	0.033	...	...

Table 2. Tail decline rates at 100, 200, and 300 days for the *U* to *K* bolometric lightcurve of SN 2011dh compared to SNe 1993J and 2008ax.

SN	Rate (100 d) (mag day^{-1})	Rate (200 d) (mag day^{-1})	Rate (300 d) (mag day^{-1})
2011dh	0.021	0.021	0.016
2008ax	0.020	0.017	0.015
1993J	0.021	0.017	0.013

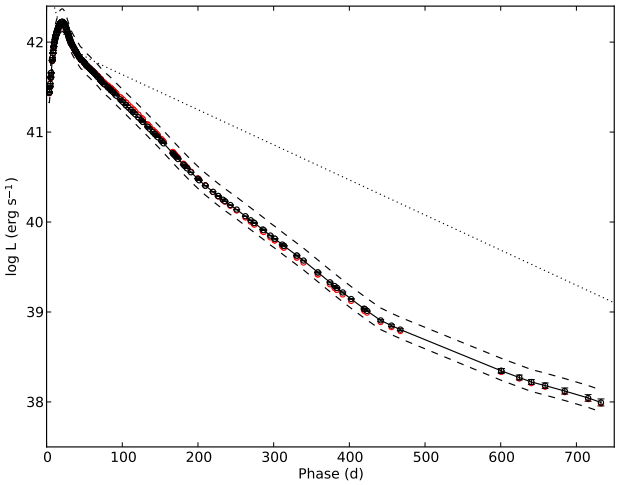

Fig. 6. Pseudo-bolometric UV to MIR lightcurve for SN 2011dh calculated with the combined spectroscopic and photometric methods (black circles and solid line). The upper and lower error bars for the systematic error arising from extinction and distance (black dashed lines) and the radioactive decay chain luminosity of 0.075 $M_\odot$ of ^{56}Ni (black dotted line) are also shown.

combined spectroscopic and photometric methods, and in Table 9 we tabulate the 3-300 days period (for which we have full UV to MIR coverage) for reference. As expected, the UV to MIR and *U* to *K* pseudo-bolometric lightcurves are very similar. The decline rates at 100, 200, 300 and 400 days are 0.021, 0.022, 0.015 and 0.016 mag day^{-1}, but the increase in decline rate between ~150 and ~200 days is not as pronounced as in the *U* to *K* pseudo-bolometric lightcurve. Given the caveats that the NIR coverage ends at ~350 days, and the sampling is sparse and the measurement errors large after ~500 days, the UV to MIR pseudo-bolometric lightcurve shows a significant flattening after ~500 days, when the decline rate decreases to a value similar to, but lower than, the decay rate of ^{56}Co.

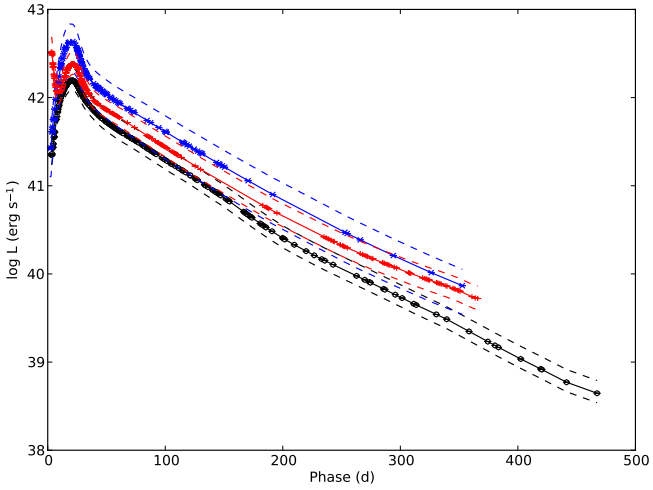

Fig. 5. Pseudo-bolometric *U* to *K* lightcurve for SN 2011dh (black circles and solid line) calculated with the photometric method as compared to SNe 1993J (red crosses and solid line) and 2008ax (blue pluses and solid line). The upper and lower error bars for the systematic error arising from extinction and distance (dashed lines) are also shown.

Figure 7 shows the fractional UV (1900-3300 Å), optical (3300-10000 Å), NIR (10000-24000 Å) and MIR (24000-50000 Å) luminosities for SN 2011dh. The early evolution was discussed in E14a, and after 100 days the most notable is the strong increase in the MIR fraction between ~100 and ~250 days. The subsequent evolution becomes quite uncertain after ~350 days when the NIR coverage ends and ~500 days when the sampling and measurement errors become worse, but the optical, NIR and MIR fractions seems to be roughly constant during this period. Keeping these uncertainties in mind it is worth noting the dominance of the optical flux even at ~750 days.

Figure 8 shows the evolution of the SED as calculated with the photometric method, overplotted with blackbody fits to the *V*, *I*, *J*, *H* and *K* photometry as well as the observed (interpolated) spectra. The early evolution was discussed in E14a, and after 100 days the most notable is again the strong excess de-

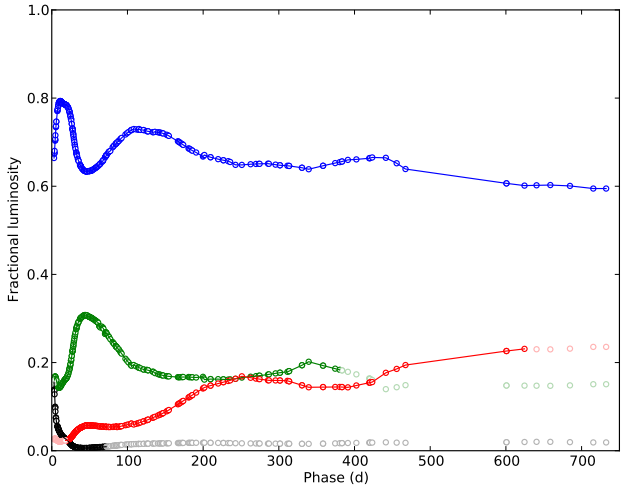

Fig. 7. Fractional UV (black dots), optical (blue dots), NIR (green dots) and MIR (red dots) luminosity for SN 2011dh. Luminosities based on extrapolated magnitudes are displayed in shaded colour.

veloping in the MIR between ∼100 and ∼250 days. There also seems to be a similar excess developing in the K band between ∼100 and ∼200 days, gradually fading away towards 300 days.

3.3. Spectroscopic evolution

Steady-state NLTE modelling of the 100-500 days spectral evolution as well as a detailed analysis of the formation of the identified lines and the evolution of their fluxes are presented in J14. In this section we summarize the findings in J14 and provide a complementary analysis, mainly related to the line profiles and what can be learned about the distribution of the material from the different nuclear burning zones. In doing this we refer to the subdivision of the (unmixed) ejecta described in J14 with a Fe/Co/He core surrounded by the Si/S zone, the oxygen-rich O/Si/S, O/Ne/Mg and O/C zones, the helium-rich He/C and He/N zones and the hydrogen-rich envelope. The amount of macroscopic mixing between these zones is determined by hydrodynamical instabilities in the explosion (Hammer et al. 2010) and is a free parameter in the steady-state NLTE modelling.

Figure. 9 shows the (interpolated) evolution of all lines identified in J14 and in Sects. 3.3.2-3.3.7 we discuss the identified lines element by element (with some exceptions) and measure the sizes of the line emitting regions and the asymmetries of the line profiles using the methods described in 3.3.1. In Sects. 3.3.9 and 3.3.10 we summarize the results, use knowledge gained in J14 to discuss the distribution of the nuclear burning material in the ejecta and compare the results to SNe 1993J and 2008ax In Sect. 3.3.11 we discuss small scale variations in the most important line profiles and constraints obtained from those on the origin of these lines and the macroscopic mixing of the nuclear burning material.

3.3.1. Methods

To estimate the sizes of the line emitting regions we fit the line profile of a spherically symmetric region of constant line emissivity, optically thin in the line and with a constant absorptive continuum opacity, to the observed line profile. The aborptive continuum opacity is included to reproduce the blue-shifts observed in some line profiles. In J14 we suggest the cause of

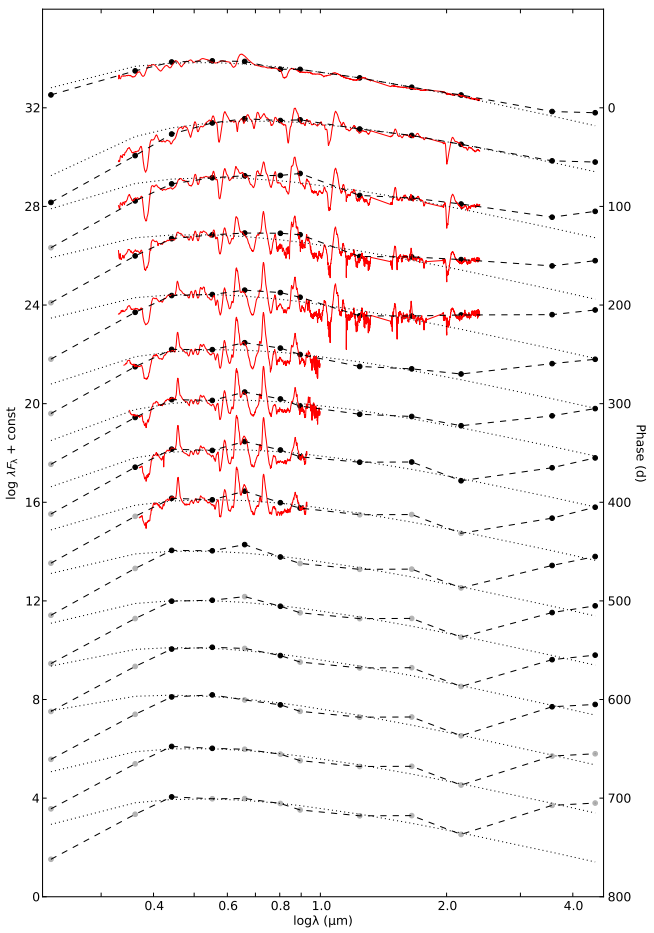

Fig. 8. The evolution of the SED as calculated with the photometric method (black dots and dashed lines) overplotted with blackbody fits to the V, I, J, H and K photometry (black dotted lines) as well as the observed spectra interpolated as described in Sect. 2.2.1 (red solid lines). Fluxes based on extrapolated magnitudes are displayed in shaded colour.

these blue-shifts to be line blocking in the core. This method gives a rough estimate of the size of the region responsible for the bulk of the line emission and is only used for lines found to be optically thin in J14.

Some lines arise as a blend of more than one line which has to be taken into account. The [O I] 6300 Å flux was calculated by iterative subtraction of the [O I] 6364 Å flux, from the left to the right, using $F_{6300}(\lambda) = F_{6300,6364}(\lambda) - F_{6300}(\lambda - \Delta\lambda)/R$, where $\Delta\lambda$ is the wavelength separation between the [O I] 6300 Å and 6364 Å lines and R the [O I] 6300,6364 Å line ratio. This ratio was assumed to be 3, as is supported by the steady-state NLTE modelling and estimates based on small scale variations (Sect. 3.3.11). In all other cases, where the line ratios of the blended lines are not known, we make a a simultaneous fit assuming the same size of the emitting region for all of the blended lines.

To estimate the assymetry of the line profiles we calculate the first wavelength moment of the flux (center of flux). The continuum level is determined by a linear interpolation between the minimum flux levels on the blue and red sides within a region set to ±6000 km s^{-1} for most of the lines, ±10000 km s^{-1} for the Ca II 8662 Å line and ±3000 km s^{-1} for the [Fe II] 7155 Å line. The rest wavelength is assumed to be 6316 Å for the

[O I] 6300,6364 Å line as is appropriate for a line ratio of 3 and 5993 Å, 7307 Å and 8662 Å for the Na I 5890,5896 Å, [Ca II] 7291,7323 Å and Ca II 8498,8542,8662 Å lines respectively.

3.3.2. Hydrogen lines

Some Hα emission arising from the hydrogen-rich envelope is present in the optimal steady-state NLTE model, but is increasingly dominated by [N II] 6548,6583 Å emission arising from the helium zone after ~150 days (J14). There is an emerging emission feature near the rest wavelength of Hα (Fig. 9) which we find to be well fitted by emission from a region with a radius of 5500 km s^{-1}, emitting mainly in the [N II] 6583 Å line, although the wings of the observed line profile may extend to ~12000 km s^{-1} on the red side. Hα emission from the hydrogen-rich envelope is expected to result in a flat-topped line profile, at least 11000 km s^{-1} wide (E14a). The size of the line emitting region, as well as the extent of the wings, is instead consistent with emission from the helium zone, in agreement with the results in J14. No detectable absorption is found in any of the hydrogen lines in the optimal steady-state NLTE model (J14). There is a dip in the [O I] 6300,6364 Å line profile after ~150 days (Figs. 9 and 10), that corresponds well to the early time Hα absorption minimum at ~11000 km s^{-1} (E14a). However, as discussed in Sect. 3.3.11, this feature repeats in a number of other lines and is rather due to clumping/asymmetries in the ejecta.

3.3.3. Helium lines

The identified helium lines are the He I 10830 Å and He I 20581 Å lines, although the He I 10830 Å line is blended with the [S I] 10820 Å line (J14). Both the He I 10830 Å and He I 20581 Å lines have P-Cygni like profiles, suggesting a significant contribution from scattering, in agreement with the results in J14. The absorption extends to ~10000 km s^{-1} for the He I 20581 Å line and a bit further for the He I 10830 Å line. This is consistent with the results in E14a where the size of the helium core was found to be ~11000 km s^{-1}. Although the unblended He I 20581 Å line has a quite broad peak it is not flat-topped, suggesting a contribution from helium at low velocities. This is consistent with the results in J14, where we find helium in the Fe/Co/He zone to contribute significantly at low velocities.

3.3.4. Oxygen lines

The identified oxygen lines are the [O I] 5577 Å, O I 7774 Å, O I 9263 Å, O I 11300 Å, O I 13164 Å and [O I] 6300,6364 Å lines, although the O I 9263 Å line is blended with the [Co II] 9338,9344 Å line on the red side (J14). Fig. 10 shows line profile fits for the decomposed [O I] 6300 Å line for SN 2011dh as compared to SNe 1993J and 2008ax. We measure the radius of the [O I] 6300,6364 Å line emitting region to 3400, 3100 and 2900 km s^{-1} at 202, 300 and 415 days respectively. The line profile fits are quite good, but the observed emission is underestimated at low velocities and extends to at least ~5000 km s^{-1}, suggesting radially decreasing emissivity. The other oxygen lines are either weak or found to be blended or optically thick in J14 so we do not attempt to estimate the sizes of their line emitting regions. The center of flux of the [O I] 6300,6364 Å line shows a blue-shift of ~1000 km s^{-1} at 100 days, decreasing towards zero at 400 days, whereas the center of flux of the [O I] 5577 Å line shows a blue-shift of ~1500 km s^{-1} at 100 days, decreasing towards ~1000 km s^{-1} at 200 days, when the line begins to fade away. We do not find any significant blue-shifts of the O I 11300 and 13164 Å lines.

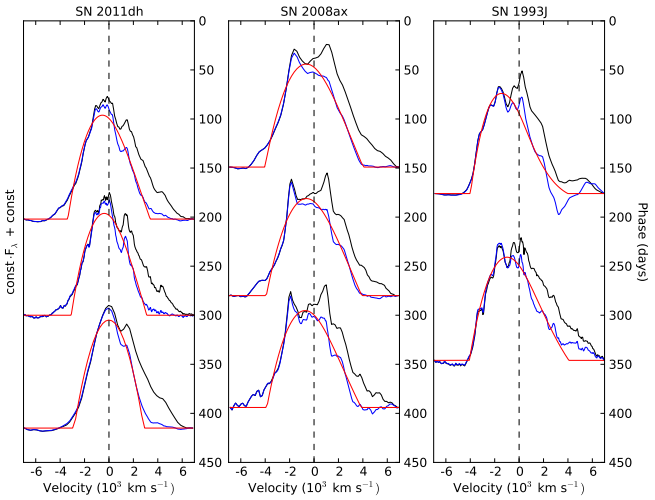

Fig. 10. [O I] 6300,6364 Å (black) and decomposed [O I] 6300 Å (blue) line profiles at selected epochs as compared to line profile fits (red) for SNe 2011dh (left panel), 2008ax (middle panel) and 1993J (right panel).

3.3.5. Magnesium lines

The identified magnesium lines are the Mg I] 4571 Å and Mg I 15040 Å lines (J14). Fig. 11 shows line profile fits for the Mg I] 4571 Å line for SN 2011dh as compared to SNe 1993J and 2008ax. We measure the radius of the Mg I] 4571 Å line emitting region to 3600, 2800 and 2700 km s^{-1} at 202, 300 and 415 days respectively, and the radius of the Mg I 15040 Å line emitting region to 3400 and 2900 km s^{-1} at 89 and 205 days respectively. The line profile fits of the Mg I] 4571 Å line are quite good, but the observed emission is underestimated at low velocities and extends to at least ~5000 km s^{-1}, suggesting radially decreasing emissivity. The center of flux of the Mg I] 4571 Å line shows a blue-shift of ~1000 km s^{-1} at ~200 days, decreasing towards a few hundred km s^{-1} at ~400 days. We do not find any significant blue-shift of the Mg I 15040 Å line.

3.3.6. Calcium lines

The identified calcium lines are the Ca II 3934,3968 Å, Ca II 8498,8542,8662 Å and [Ca II] 7291,7323 Å lines, although the the Ca II 8498,8542,8662 Å line is blended with the [C I] 8727 Å line (J14). Fig. 12 shows two-component line profile fits for the [Ca II] 7291,7323 Å line for SN 2011dh as compared to SNe 1993J and 2008ax. We measure the radii of the [Ca II] 7291,7323 Å line emitting regions to 2400/9900, 2100/9100 and 2400/9000 km s^{-1} at 202, 300 and 415 days respectively. The line profile fits are good in the inner region but worse in the wings, which are quite asymmetric and also blended with the [Fe II] 7155 Å line on the blue side. The fitted two-component line profile is consistent with the results in J14 where we found the [Ca II] 7291,7323 Å lines to arise mainly from the Si/S zone, with a possible contribution from fluorescence throughout the ejecta. The more pronounced red-side wing of the broad component rather sug-

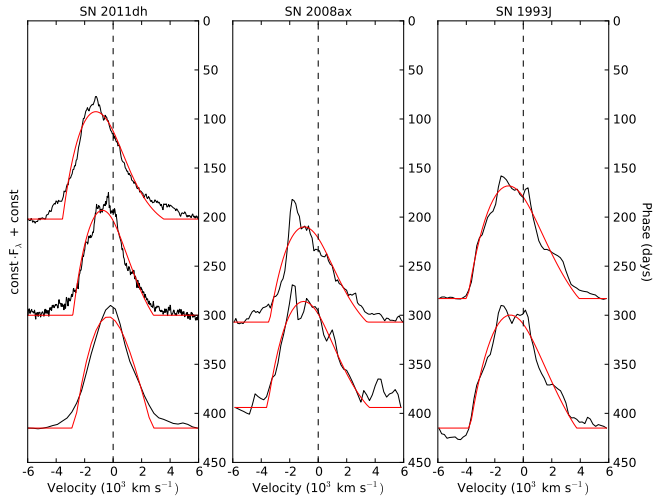

Fig. 11. Mg I] 4571 Å line profiles (black) at selected epochs as compared to line profile fits (red) for SNe 2011dh (left panel), 2008ax (middle panel) and 1993J (right panel).

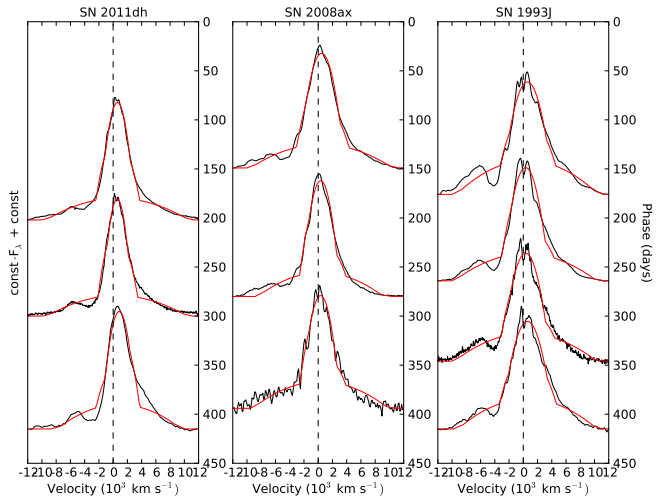

Fig. 12. [Ca II] 7291,7323 Å line profiles (black) at selected epochs as compared to line profile fits (red) for SNe 2011dh (left panel), 2008ax (middle panel) and 1993J (right panel).

gest this to arise from scattering though. The center of flux for the Ca II 8498,8542,8662 Å line shows a red-shift increasing towards ∼1000 km s^{-1} at 400 days. As the center of flux is calculated with respect to the rest wavelength of the Ca II 8662 Å line (Sect. 3.3.1) this suggests a significant contribution from the [C I] 8727 Å line to the flux. In J14 we found the [C I] 8727 Å line to arise mainly from the O/C zone, so this is in agreement with a scenario where the amount of molecule (CO) cooling in the C/O zone is modest.

3.3.7. Iron group lines

The identified iron lines are the [Fe II] 7155 Å, [Fe II] 12600 Å and [Fe II] 16400 Å lines (J14). The identified cobalt lines are the [Co II] 9338,9344 Å, [Co II] 10190,10248,10283 Å and [Co II] 15475 Å lines, although the [Co II] 9338,9344 Å line is blended with the O I 9263 Å line on the blue side (J14). We measure the radius of the [Fe II] 7155 Å line emitting region to 1600 km s^{-1} at 300 and 415 days, and the radius of the [Fe II] 16440 Å line emitting region to 2100 km^{-1} at 206 days. We also measure the radius of the [Co II] 10190,10248,10283 Å line emitting region to 2000 km s^{-1} at 206 days. The [Co II] 15475 Å line is noisy, but we find the radius of the line-emitting region to be 3200 km s^{-1} at 206 days. As mentioned the [Co II] 9338,9344 Å line is blended with the O I 9263 Å line on the blue side, and also appears to be blended with other lines on the red side, so we do not attempt to estimate the radius of the line emitting region.

3.3.8. CO emission

Figure 13 shows continuum subtracted observed K band spectra at 89 and 206 days compared to the synthetic K band spectrum at 200 days for the optimal steady-state NLTE model (Sect. 4.1). The region where we expect CO overtone emission is marked in the figure and is assumed to be 22750-24350 Å (reference). The continuum was estimated as a linear interpolation between the endpoint fluxes of the region averaged over 100 Å. As seen in Fig. 13 there is a clear excess in the region both compared to the continuum and the model spectrum and the shape and extent of the feature is similar at 89 and 202 days. Although other explanations cannot be excluded we find it reasonable to interpret this feature as CO overtone emission. The integrated continuum subtracted flux in the region was 3.1×10^{-14} and 8.1×10^{-15} erg s^{-1} cm^{-2} at 89 and 206 days respectively. These values should be taken with some caution as they depend sensitively on the method used to subtract the continuum.

The region where we expect CO fundamental band emission overlaps with the 4.5 μm band. As discussed in E14a, there is an excess in this band developing during the first hundred days, as compared to blackbody fits to the optical and NIR photometry. As seen in Fig. 8, this excess continues to develop after 100 days, and at 600 days the 4.5 μm band is ∼100 times brighter as compared to such a blackbody fit. The total flux in the 4.5 μm band, calculated using the zeropoint flux and the equivalent width of the band, was 4.9×10^{-13} and 1.7×10^{-13} erg s^{-1} cm^{-2} at 89 and 206 days respectively. Note that the value at 206 days lies in the gap of the Spitzer observations and has been linearly interpolated between 85 and 251 days. If all of the flux in the 4.5 μm band was due to CO fundamental band emission this would correspond to fundamental to first overtone band flux ratios of ∼15 and ∼20 at 85 and 206 days respectively.

On the other hand the SiO overtone band and dust may also contribute to the 4.5 μm band so we cannot assume that all of the observed flux is due to CO fundamental band emission. Knowledge of the CO fundamental to first overtone band flux ratio would make an estimate of the contribution from CO fundamental band emission to the 4.5 μm flux possible. For SN 1987A this ratio was ∼1 at 100 days, a few at 200 days, but increased dramatically to ∼100 towards 500 days (Bouchet & Danziger 1993). So assuming the same flux ratios as for SN 1987A would suggest a minor contribution to the 4.5 μm flux from CO fundamental band emission at these epochs. However, this assumption is a bit dubious as the mass, density and composition of the ejecta are quite different for a Type IIb SN as compared to SN 1987A.

3.3.9. Line emitting regions

In Sects. 3.3.4, 3.3.5, 3.3.6 and 3.3.7 we estimate the sizes of the O I, Mg I, [Ca II] 7291,7323 Å, Fe II and Co II line emitting regions for SN 2011dh and in Figs. 10, 11 and 12 we show the corresponding line profile fits for the [O I] 6300 Å, Mg I]

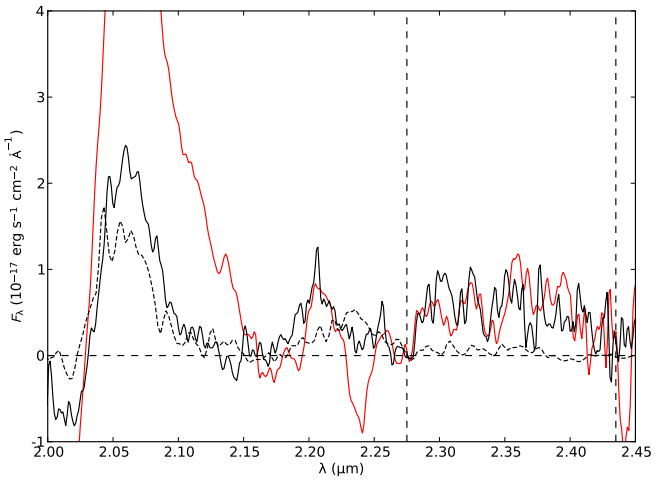

Fig. 13. Continuum subtracted observed *K* band spectra at 89 (red solid line) and 206 (black solid line) days compared to the continuum subtracted synthetic *K* band spectrum at 200 days (black dashed line) for the optimal steady-state NLTE model. The CO overtone region have been marked by black dashed lines and the observed flux at 89 days scaled with the ratio of the measured total CO overtone fluxes.

4571 Å and [Ca II] 7291,7323 Å lines for SN 2011dh, 2008ax and 1993J. Figure 14 shows overplotted continuum subtracted mirrored blue-side profiles for the [O I] 6300 Å, Mg I] 4571 Å, [Ca II] 7291 Å and [Fe I] 7155 Å lines for SNe 2011dh, 2008ax and 1993J at 300, 307 and 283 days respectively. The blue side is less affected by obscuration as compared to the red side and contamination from the [O I] 6364 Å and [Ca II] 7323 Å lines to the [O I] 6300 Å and [Ca II] 7291 Å lines is probably modest, although the [Ca II] 7291,7323 Å line ratio is uncertain.

As mentioned, in J14 we find the Mg I lines to arise from the O/Ne/Mg zone, the O I lines to arise from the O/Ne/Mg zone and, depending on the amount of molecule (CO and SiO) cooling, the O/C and O/Si/S zones, the [Ca II] 7291,7323 Å line to arise mainly from the Si/S zone and the Fe II and Co II lines to arise from the Fe/Co/He zone. The estimated radii of the Mg I and O I line emitting regions are similar whereas the blue-side lines profiles are remarkably similar, suggesting these to arise from the O/Ne/Mg/Zone. The estimated radii of the [Ca II] 7291,7323 and the Fe II and Co II line emitting regions are progressively smaller, suggesting partial mixing of the O/Ne/Mg, Si/S and Fe/Co/He material.

For SNe 1993J the estimated radii of the line emitting regions are 4000-4100 km s^{-1} for the [O I] 6300 Å line, 3700-3900 for the Mg I] 4571 Å line and 3000-3400 km s^{-1} for the [Ca II] 7291,7323 Å line. For SNe 2008ax the estimated radii of the line emitting regions are 3900-4000 km s^{-1} for the [O I] 6300 Å line, 3400-3600 km s^{-1} for the Mg I] 4571 Å line and 2600-3000 km s^{-1} for the [Ca II] 7291,7323 Å line. These radii are larger than those estimated for SN 2011dh and larger for SN 1993J than for SN 2008ax. The radii of the Mg I] 4571 Å and the [O I] 6300 Å lines are are similar and the blue-side line profiles are remarkably similar, suggesting these to arise from the O/Ne/Mg zone. The radius of the [Ca II] 7291,7323 Å line emitting region is smaller than the radii of the [O I 6300] Å and Mg I] 4571 Å line emitting regions, suggesting partial mixing of the O/Ne/Mg and Si/S material. It is also evident from Fig. 14 that there is considerable differences in the shapes of line profiles.

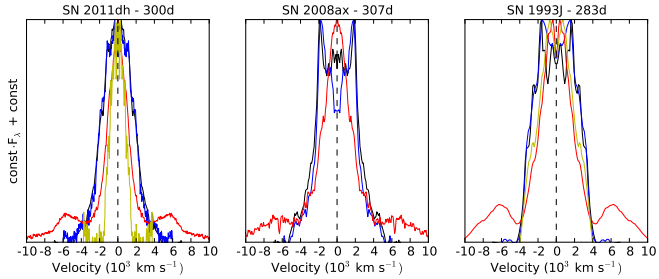

Fig. 14. Continuum subtracted mirrored blue-side profiles for the [O I] 6300,6364 Å (black), Mg I] 4571 Å (blue), [Ca II] 7291,7323 Å (red) and [Fe I] 7155 Å (yellow) lines for SNe 2011dh, 2008ax and 1993J at 300, 307 and 283 days respectively.

The profile of the [Ca II] 7291,7323 Å line is centrally peaked for all three SNe whereas the peaks of the [O I 6300] Å and Mg I] 4571 Å line are considerably flatter for SNe 1993J and 2008ax. A thourough discussion of this issue is outside the scope of the paper however, and has to be postponed to future works.

3.3.10. Line asymmetries

Figure 15 shows the center of flux velocities for the [O I] 6300,6364 Å, [O I] 5577 Å, Mg I] 4571 Å and [Ca II] 7291,7323 Å lines for SNe 2011dh, 2008ax and 1993J. As discussed in Sects. 3.3.4 and 3.3.5 there is a blue-shift of the [O I] 6300,6364 Å, [O I] 5577 Å and Mg I] 4571 Å lines for SN 2011dh which, as seen in Fig. 15, is also present, and even more pronounced for SNe 2008ax and 1993J. For SN 2011dh this blue-shift disappears towards 400 days but for SNe 2008ax and 1993J the blue-shift saturates at ∼500 km s^{-1} after 200 days. In J14 we provide a thorough discussion of these blue-shifts and suggest the cause to be line-blocking in the core based on results from the steady-state NLTE modelling. There is no significant blue shift in the O I 11300 Å, O I 13164 Å and [Mg I] 15040 Å lines for SNe 2011dh (Sects. 3.3.4 and 3.3.5) and 2008ax in support of this hypothesis, as line-blocking is less effective in the NIR (J14). Milisavljevic et al. (2010) find the [O I] 6300,6364 Å, [O I] 5577 Å and Mg I] 4571 Å lines to be either symmetric or asymmetric towards the blue for a sample of 18 stripped envelope SNe whereas Taubenberger et al. (2009) find a systematic blue-shift of the [O I] 6300,6364 Å line disappearing with time for another, partly overlapping, sample of 39 stripped envelope SNe. Both these results favours obscuration of the receding-side emission and disfavours ejecta asymmetries as the explanation, whereas the latter result is in agreement with our results for SN 2011dh and disfavours obscuration by dust. However, to explain the saturation of the blue-shifts for SNe 2008ax and 1993J the evolution of the core-opacity needs to be different for these SNe as compared to SN 2011dh.

As a further complication blue-shifts of the lines profiles could also be produced by dust in the ejecta. Using our line profile model and assuming a size of the line-emitting region of 3000 km s^{-1}, roughly corresponding to size of the oxygen zone for SN 2011dh, we find a blue-shift of the center of flux of ∼150 km s^{-1} for an optical depth of 0.25. This amount of dust is found to reproduce the increase in the decline rates of the optical pseudo-bolometric lightcurve observed between 100 and 200 days (Sect. 4.1.6). However, the change in optical depth due to dust and line blocking is hard to disentangle, most lines

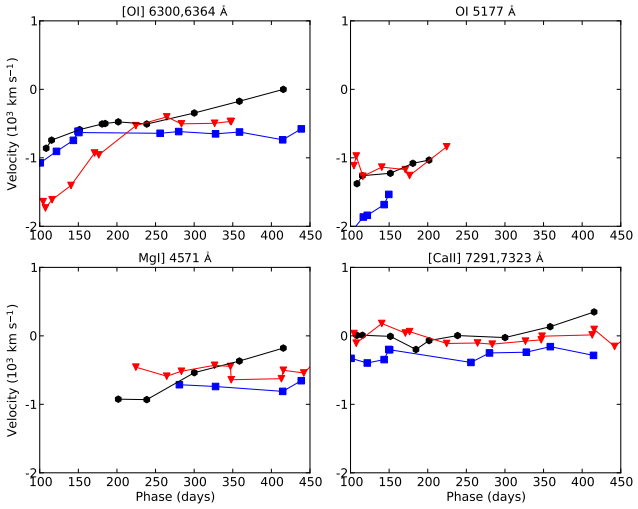

Fig. 15. Center of flux velocities for the [O I] 6300,6364 Å (upper left panel), [O I] 5577 Å (upper right panel) Mg I] 4571 Å (lower left panel), [Ca II] 7291,7323 Å (lower right panel) lines for SNe 2011dh (black dots), 2008ax (blue squares) and 1993J (red triangles).

are either blends, do not arise solely from the core or are too weak and if the dust is located differently the effect on the line profiles would be different. At 415 days, when the effect from line-blocking would be the least, the center of flux for the [O I] 6300,6364 Å and Mg I] 4571 Å lines, which arises solely from the core, are ∼50 and ∼200 km s^{-1} respectively. The small blue-shift of the former indicates that if dust is formed in the ejecta it is not homogenously distrubuted within the core. For SNe 1993J and 2008ax dust in the ejecta provides an alternative explanation for the saturation of the blue-shifts. Using our line profile model and assuming a size of the line-emitting region of 4000 km s^{-1}, roughly corresponding to size of the oxygen zone for SNe 1993J and 2008ax, we find a blue shift of the center of flux of ∼500 km s^{-1} to correspond to an optical depth of ∼1. Neither SN 1993J nor SN 2008ax show a period with increased decline rates in the optical pseudo-bolometric lightcurve which disfavours dust as the explanation, although SN 1993J show a MIR excess developing between 100 and 250 days, similar to that observed for SN 2011dh.

3.3.11. Small scale fluctuations

Small scale fluctuations in the line profiles may provide evidence for a clumpy ejecta as have been previously demonstrated for SNe 1993J (Matheson et al. 2000) and 1987A (Stathakis et al. 1991; Chugai 1994). In a simplified way we may represent the material of some nuclear burning zone by a number of randomly distributed clumps, having a typical size and occupying some fraction of the ejecta volume (filling factor). The small scale fluctuations in the line profiles then arise from statistical fluctuations in the distribution of the clumps, the RMS of the fluctuations increasing with decreasing number of clumps and/or filling factor and/or increasing size of the clumps. In the simplest case the ejecta is assumed to be a (globally) homogeneous sphere, which is in fact exactly how the core is represented in the steady-state NLTE modelling (Sect. 4.1).

Figure 16 shows small scale fluctuations in the [O I] 6300,6364 Å, [O I] 5577 Å, O I 7774 Å, Mg I] 4571 Å and Na I 5890,5896 Å lines at 202 and 300 days. The resolution is ∼600 and ∼250 km s^{-1} in the 202 and 300 days spectra respectively. A 1000 km s^{-1} box average of the line profile was repeatedly (3 times) subtracted to enhance the small scale fluctuations. The method have been tested on the product of synthetic large and small scale structures and the small scale structure is recovered with reasonable accuracy. In the upper left panel we show a comparison of the [O I] 6300 Å line profiles at 202 and 300 days. These are very similar and there is not much evolution of the small scale fluctuations in the line profile during this period. We identify 8 features marked A-H with an FWHM between 300 and 600 km s^{-1} present at both epochs. However, features G and H interpreted as belonging to the [O I] 6364 Å line match very well with the E and F features interpreted as belonging to the [O I] 6300 Å line so these are likely to be repetitions. Minimizing the RMS (Root Mean Square) of the small scale fluctuations redwards 3000 km s^{-1} (G and H), where the [O I] 6364 Å flux was subtracted from the [O I] 6300,6364 Å line profile using the method described in Sect. 3.3.1, we find a line ratio of 2.9 at 202 and 300 days to give a complete removal of features G and H. This ratio is in agreement with the value of 3 expected for optically thin emission and also with the results from J14.

In the upper right panel we show the corrected [O I] 6300 Å line profile and in the lower left panel we show a comparison to the Mg I] 4571 Å line profile at 300 days. All features except B are clearly identified and the agreement is good. The features on the red side are weaker for the Mg I] 4571 Å line, which is consistent with the larger red-side flux deficit for this line, but the relative (flux normalized) strength of all features are similar. The good agreement suggests that the [O I] 6300 Å and Mg I] 4571 Å lines arise from the same nuclear burning zones. Given that the Mg I] 4571 Å line arises mainly from the O/Ne/Mg zone, as found in J14, it also suggests that the [O I] 6300 Å line arises mainly from this zone and that the contribution from the O/Si/S and O/C zones are modest. In the lower right panel we show a comparison of the corrected [O I] 6300 Å line profile and the [O I] 5577 Å, O I 7774 Å and Na I 5890,5896 Å line profiles at 202 days. The E and F features are clearly identified in all of these line profiles, but none of the other features are seen. Since the E and F features are also the strongest it is not clear if the absence of the other features is real or if the other features are just too faint to be seen. The relative strength of the E and F features are similar for the [O I] 5577 Å, O I 7774 Å and [O I] 6300 Å lines, suggesting that all these lines arise mainly from the same nuclear burning zones, whereas the relative strength of these features for the Na I 5890,5896 Å line is a bit (∼50 percent) weaker, suggesting contributions from other nuclear burning zones. This is in agreement with the results in J14, where all oxygen lines are found to arise from the oxygen zones and the Na I 5890,5896 Å line partly from the O/Ne/Mg zone.

The small scale fluctuations in the [Ca II] 7291,7323 Å line (not shown) do not match very well with those in the [O I] 6300 Å line and the relative strength of the features seen is weaker. We were not able to correct for blending as for the [O I] 6300,6364 Å line, which makes the interpretation less clear, but the result is in agreement with the results in J14, were we found this line to arise from other nuclear burning zones. This is also suggested by the different sizes of the line emitting regions discussed in Sect. 3.3.6.

Shivvers et al. (2013) presented an analysis of the line profiles of the [O I] 6300,6364 Å, O I 7774 Å and Mg I 4571 Å lines at 268 days. By decomposition of the [O I] 6300,6364 Å line pro-

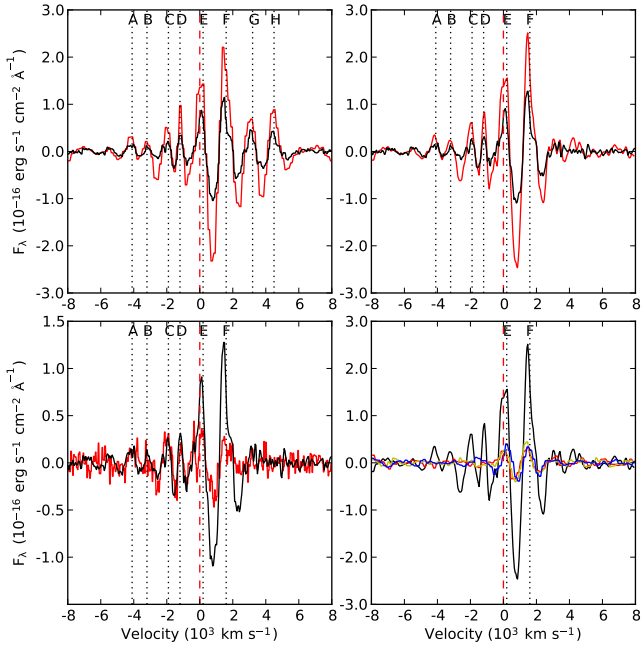

Fig. 16. Comparison of box average subtracted line profiles. The upper left panel shows the [O I] 6300 Å line profile at 202 (red) and 300 (black) days. The upper right panel shows the corrected [O I] 6300 Å line profile at 202 (red) and 300 (black) days. The lower left panel shows the corrected [O I] 6300 Å line profile (black) and the Mg I] 4571 Å line profile (red) at 300 days. The lower right panel shows the corrected [O I] 6300 Å line profile (black) and the [O I] 5577 Å (red), O I 7774 Å (green) and Na I 5890/5896 Å (blue) line profiles at 202 days.

file into Gaussian profiles, assuming an [O I] 6300,6364 Å line ratio of 3, they found a good fit for one broad and two narrow profiles located at -400 and 1600 km s^{-1}. The two strongest features in our analysis, E and F, are located at ∼0 and ∼1500 km s^{-1} and likely correspond to the two features found by Shivvers et al. (2013). They also find these features to repeat in the O I 7774 Å and Mg I 4571 Å lines, in agreement with our analysis. The difference in velocity for the E feature is likely explained by the different methods used.

Matheson et al. (2000) presented an analysis of the small scale fluctuations in the line profiles of SN 1993J. They found a good agreement between the fluctuations in the [O I] 6300 Å, [O I] 5577 Å and O I 7774 Å line profiles, which is in agreement with our results for SN 2011dh. However, they did not find a good agreement between the fluctuations in the [O I] 6300 Å and Mg I] 4571 Å line profiles, which is a bit surprising since we find an excellent agreement between fluctuations in these lines for SN 2011dh. One possible explanation is that the [O I] 6300 Å line is dominated by flux from the O/Ne/Mg zone for SN 2011dh but not for SN 1993J, as we expect the Mg I] 4571 Å line to emerge from this zone, whereas the oxygen lines could also have contributions from the O/Si/S and O/C zones.

Matheson et al. (2000) applied the statistical model by Chugai (1994) to their spectra of SN 1993J, giving a filling factor of ∼0.06 for oxygen zone material, distributed within a sphere with 3800 km s^{-1} radius. Using their estimated typical clump size of 300 km s^{-1}, this corresponds to ∼900 clumps. The model requires the radius of the sphere containing the clumps, the typical size of the clumps and the RMS of relative flux fluctuations in lines originating from the clumps. In the case of SN 2011dh we adopt a radius of the sphere containing the bulk of the oxygen zone material of ∼3500 km s^{-1} based on the estimates of the O I and Mg I line emitting regions in Sect. 3.3.4 and 3.3.5. For SN 1987A a typical clump size of 120 km s^{-1} was estimated from the power spectrum of the [O I] 6300 Å line by Stathakis et al. (1991) using high-resolution spectroscopy, but it is not clear how this was done by Matheson et al. (2000). As we do not have access to high-resolution spectroscopy for SN 2011dh we can only estimate an upper limit on the typical clump size taken to be 300 km s^{-1}, the smallest size of the features seen. The RMS of the relative flux fluctuations in the inner part (±2000 km s^{-1}, see Chugai (1994)) of the sphere for both the corrected [O I] 6300 Å and the Mg I 4571 Å lines was ∼0.09 at 300 days. Using these estimates and applying Chugai (1994, eq. 11), we find an upper limit on the filling factor of oxygen zone material within the sphere of ∼0.07 and a lower limit on the number of oxygen zone clumps of ∼900. These values are in good agreement with the values estimated by Matheson et al. (2000) for the clumping of oxygen zone material in SN 1993J.

4. Modelling

In this section we discuss modelling of the bolometric and photometric lightcurves with the steady-state NLTE code described in Jerkstrand et al. (2011, 2012) and J14 and HYDE, a hydrodynamical code described in E14b. HYDE, which is based on the diffusion approximation and Rossland mean opacities, can only produce bolometric lightcurves, whereas the steady-state NLTE code, which solves the frequency dependent radiative transfer, is capable of producing photometric and pseudo-bolometric lightcurves. HYDE, on the other hand, has the hydrodynamical and time-dependent capabilities needed to evolve the SN through the explosion and the diffusion phase, whereas steady-state NLTE code has not and can only be used at times later than ∼100 days. In the tail phase, where the diffusion time is short and steady-state is satisfied, both codes have the capability to produce bolometric lightcurves and in fact use the same radiative transfer model to calculate the deposition of the radioactive decay energy. So the advantage of the steady-state NLTE code is the capability to calculate pseudo-bolometric and photometric lightcurves or, equivalently, the corresponding bolometric corrections.

Given the extensive coverage for SN 2011dh, both in time and wavelength, consistent modelling of the bolometric and photometric lightcurves, throughout the evolution, is highly desirable. Ideally, HYDE would be used to evolve a grid of initial stellar models through a parametrized explosion and the photospheric phase, and the resulting ejecta models then fed into the steady-state NLTE code and subsequently evolved. The resulting grid of SN models could then be fitted to observations and the degeneracy of the solution and the errors in the parameters quantified. For the 0-100 days evolution we use the grid of SN models, constructed with HYDE and MESA STAR, presented in E14b, but to evolve this 15×10×9×9 grid further with the steady-state NLTE code is not computationally feasible. We are therefore forced to use the hydrodynamical grid for the early evolution (0-100 days) and a highly restricted set of steady-state NLTE models, presented in J14, for the late evolution (100-500 days). To partly circumvent this problem we try two different approaches. First, to extend the temporal coverage of the J14 models to early times, we evolve these through the 0-100 days period using HYDE in homologous mode. Secondly, to extend the temporal coverage of the hydrodynamical model grid to 300 days,

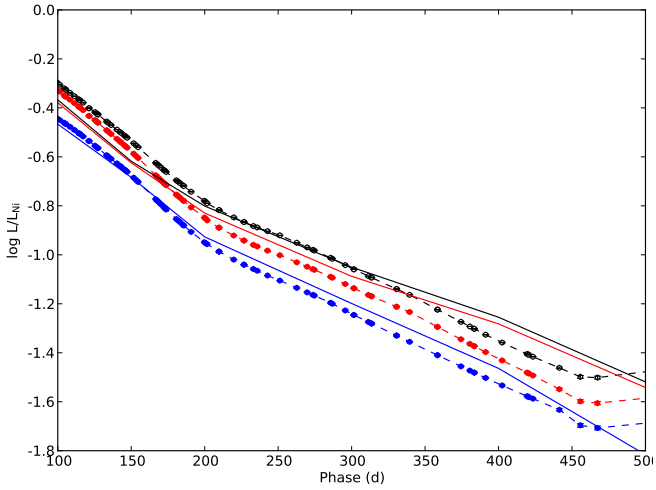

Fig. 17. 100-500 days U to 4.5 μm (black lines), U to K (red lines) and U to z (blue lines) bolometric lightcurves for the optimal model (12C) as compared to the observed U to 4.5 μm (black circles), U to K (red circles) and U to z (blue circles) bolometric lightcurves. The lightcurves have been normalized to the radioactive decay chain luminosity of 0.075 $M_\odot$ of ^{56}Ni.

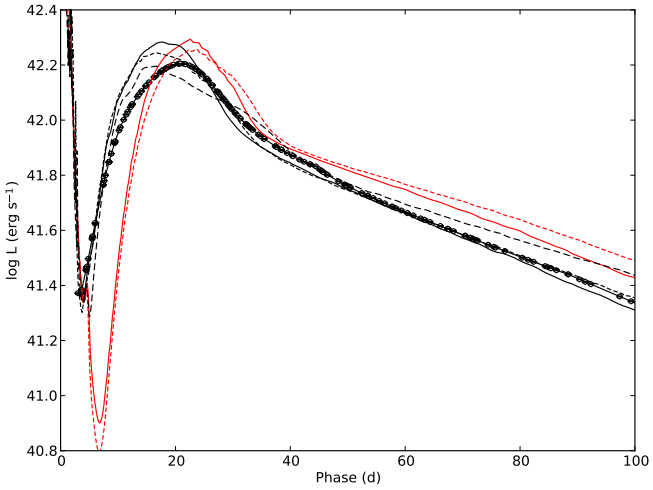

Fig. 18. 0-100 days bolometric lightcurves for the J14 models calculated with HYDE as compared to the observed U to 4.5 μm bolometric lightcurve for the first 100 days. The models are displayed as in Fig. 20.

we apply a bolometric correction determined with the steady-state NLTE code. Finally, as discussed in Sect. 4.4, after 500 days time-dependent effects becomes important and a steady-state assumption is no longer valid, so in this phase neither code apply.

4.1. NLTE modelling of the 100-500 days bolometric and photometric lightcurves

Here we compare the pseudo-bolometric and photometric lightcurves for the J14 steady-state NLTE models to the observed 100-500 days pseudo-bolometric and photometric lightcurves. Contrary to the hydrodynamical model grid used in Sects. 4.2 and 4.3, these models spans a restricted volume of parameter space and the degeneracy of the solution and the errors in the model parameters can not be quantified. The optimal model, presented in J14, have been chosen to give the best agreement with both nebular spectra and the bolometric and photometric lightcurves. In J14 we discuss the constraints on the model parameters provided by the nebular spectra and here we discuss the constraints provided by the bolometric and photometric lightcurves. The set of models, listed in table 2 in J14, varies in at least one of the following parameters, initial mass (12, 13 or 17 $M_\odot$), degree of macroscopic mixing (medium or strong), positron trapping (local or free-streaming), molecule cooling (yes or no), dust absorption/emission (yes or no) and oxygen zone filling factor (small-large). The optimal model (12C) has an initial mass of 12 $M_\odot$, strong macroscopic mixing, local positron trapping, no molecule cooling, dust absorption/emission and an oxygen zone filling factor of 0.043. The meaning of each parameter and the different configurations used are described in detail in J14.

All J14 models have the same density profile, partly based on hydrodynamical modelling (B12) and the interfaces between the core, the helium and the hydrogen envelope are fixed in velocity space based on observations and modelling (B12; E14a, this paper). The abundances varies with initial mass as given by Woosley & Heger (2007) and the mass of ejected ^{56}Ni is fixed to 0.075 $M_\odot$ based on hydrodynamical modelling (B12, this paper). As the J14 models have been artificially constructed and have not been evolved through the 0-100 days evolution, we use HYDE in homologous mode to produce bolometric lightcurves for this phase and compare to the observed U to 4.5 μm pseudo-bolometric lightcurve. When doing this the J14 models are first rescaled to day one and then evolved using an initial temperature profile adopted from a hydrodynamical model similar to the He4R270 model in B12. In this model homology is reached and the thermal explosion energy gets exhausted at ~3 days, so the assumptions made are not critical for the subsequent evolution.

Figure 17 shows the 100-500 days optimal model and observed pseudo-bolometric lightcurves. The pseudo-bolometric lightcurves of the optimal model shows a good agreement with observations until ~300 days, where our NIR coverage ends, the differences being $\lesssim$10 percent. During the 300-500 days period the U to z pseudo-bolometric lightcurve shows a continued good agreement whereas the differences in the U to K and U to 4.5 μm pseudo-bolometric lightcurves slowly increase. Given the uncertainty in the extrapolations of the NIR photometry this is not too worrying. Fig. 18 shows the 0-100 days bolometric lightcurves for the J14 models calculated with HYDE compared to the observed U to 4.5 μm pseudo-bolometric lightcurve. The bolometric lightcurve for the optimal model shows an overall agreement, although the peak is overproduced by ~20 percent. Finally, Fig. 19 shows the U to 4.5 μm lighcurves for the J14 models compared to the observed lightcurves. The lightcurves for the optimal model show an overall agreement with observations but there are some notable exceptions, in particular the MIR bands, which we discuss further in Sect. 4.1.5.

The pseudo-bolometric luminosity may be written as $L=L_{Bol}\ 10^{0.4BC}$, where L_{Bol} is the bolometric luminosity, depending only on the deposition of radioactive decay energy and BC is the bolometric correction, depending on how this energy is processed. As mentioned, the first factor could as well be calculated with HYDE, and it is the ability to determine the second factor that is the strength of the steady-state NLTE code. The split of the pseudo-bolometric lightcurves in two factors that depend in different ways on the model parameters is also very useful for the analysis. Fig. 20 shows the 100-500 days bolometric lightcurves, calculated with HYDE, and Fig. 21 the U to 4.5 μm, U to K and U to z bolometric corrections for the J14 models. As the bolometric lightcurves depends only on the en-

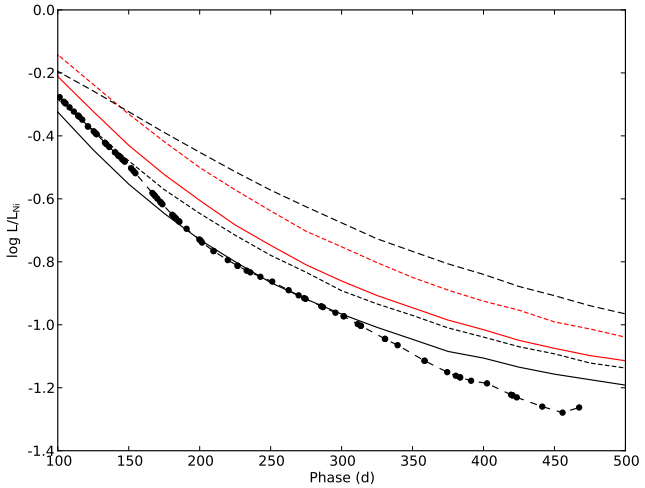

Fig. 20. 100-500 days bolometric lightcurves for the J14 models calculated with HYDE as compared to the observed bolometric lightcurve (black circles), calculated from the observed U to 4.5 μm pseudo-bolometric lightcurve using the bolometric correction for the optimal model (12C). The bolometric lightcurves have been normalized to the radioactive decay chain luminosity of 0.075 $M_\odot$ of ^{56}Ni and the displayed models are as follows; 12A (red solid line), 12BCD (black solid line), 13AB (red short-dashed line), 13CDEFG (black short-dashed line), 17A (black long-dashed line).

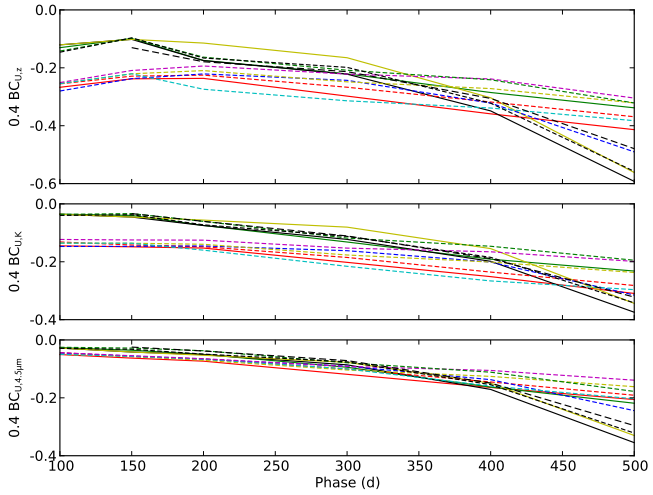

Fig. 21. 100-500 days U to 4.5 μm, U to K and U to z bolometric corrections for the J14 models. The bolometric corrections have been multiplied with 0.4 to be on the same scale as the bolometric lightcurves in Fig. 20 and the displayed models are as follows; 12A (red solid line), 12B (green solid line), 12C (black solid line), 12D (yellow solid line), 13A (red short-dashed line), 13B (blue short-dashed line), 13C (yellow short-dashed line), 13D (cyan short-dashed line), 13E (magenta short-dashed line), 13F (green short-dashed line), 13G (black short-dashed line), 17A (black long-dashed line).

ergy deposition and they are independent of molecule cooling and dust emission/absorption, which only affects the processing of the deposited energy. As we discuss below, in the J14 models, the bolometric lighturves are independent of the filling factors and the positron trapping as well. Therefore these depend only on the intial mass and the degree of macroscopic mixing, whereas the bolometric corrections may depend on all model parameters. The U to 4.5 μm bolometric corrections show very small differences (~0.05 mag) during the 100-300 days period, but these subsequently increase towards ~0.5 mag at 500 days. The U to K and U to z bolometric corrections, on the other hand, show much larger differences, mainly because molecule cooling and dust absorption/emission affects the distribution of the flux between these wavelength ranges and the MIR. Below we discuss the effects of the model parameters on the bolometric lightcurves and bolometric corrections as well as the photometric lightcurves and the constraints these provide on our choice of optimal model.

4.1.1. Initial mass

The initial mass may affect both the energy deposition (bolometric lightcurve) and the way this energy is processed (bolometric correction). Comparing the bolometric lightcurves and bolometric corrections for the optimal model (12C) and models 13G and 17A, which differs only in the initial mass, we find that the effect on the bolometric lightcurve, and thus on the energy deposition, is by far the most important. The effect of the initial mass on the bolometric lightcurve is better investigated using the hydrodynamical model grid and is discussed in detail in E14b. There we also discuss the issue of degeneracy between the model parameters, which can not be constrained by the restricted set of steady-state NLTE models. The choice of the initial mass is mainly motivated by the agreement with nebular spectra discussed in J14, but it is clear that compared to the 17 $M_\odot$ model (17A) the optimal 12 $M_\odot$ model (12C) gives a considerably better fit to the bolometric lightcurve.

4.1.2. Macroscopic mixing

The degree of macroscopic mixing may affect both the energy deposition (bolometric lightcurve) and the way this energy is processed (bolometric correction). Comparing models 13A and 13C, which differs only in the degree of macroscopic mixing and the oxygen filling factor, we find that the effect on the bolometric lightcurve, and thus on the energy deposition, is by far the most important. The mixing of the Fe/Co/He zone, containing the ^{56}Ni and its decay products, determines the overall deposition of the radioactive decay energy in the ejecta. The mixing of the other zones determines the distribution of this energy in each of these zones, which does not affect the bolometric lightcurve. We have used two configurations, one where all core zones are randomly mixed within 3500 km s^{-1} (medium), and one that differs only in that 50 percent of Fe/Co/He material have been mixed into the helium envelope within 3500-6000 km s^{-1} (strong). The effect of the mixing of Fe/Co/He material on the bolometric lightcurve is better investigated using the hydrodynamical model grid and is discussed in detail in E14b. The choice of strong mixing is mainly motivated by the lightcurve and in particular the rise to peak luminosity which is much better reproduced by models with strong mixing. Clearly there is a large number of possible configurations that have not been investigated, e.g. a configuration with partial mixing of the core zones, as we found evidence for in Sect. 3.3.

4.1.3. Filling factors

The filling factors may affects both the energy deposition (bolometric lightcurve) and the way this energy is processed (bolometric correction). However, in the J14 models the energy deposition is independent of the filling factors as the optical depths

to γ-rays and free-streaming positrons for individual Fe/Co/He clumps are $\ll$1 at times when these are contributing substantially to the energy deposition. Furthermore, there is reasons to suspect that the differences in the bolometric corrections are small as well as the fraction of the deposited energy going into heating, ionization and excitation is not particularly sensitive to the density (Kozma & Fransson 1992). We have used a number of configurations, where the filling factor of the oxygen zones ranges from small (0.043) to large (0.19), and adjusted the filling factors of the other zones accordingly. Comparing the bolometric corrections of models 13C and 13E, which differ only in the oxygen zone filling factor, these are indeed very similar, but show a small difference increasing with time, being at most ∼10 percent. The choice of a small oxygen zone filling factor is motivated by the agreement with nebular spectra discussed in J14 and is also consistent with the upper limit of ∼0.07 derived from small scale fluctuations in the [O I] 6300 and Mg I] 4571 Å lines in Sect. 3.3.11. Again there is a large number of possible configurations that have not been investigated.

4.1.4. Positron trapping

The positron trapping may affect both the energy deposition (bolometric lightcurve) and the way this energy is processed (bolometric correction). However, in the J14 models the energy deposition is independent on the positron trapping as the optical depths to free-streaming positrons are $\gg$1. Positron trapping only affects the bolometric corrections when the fraction of radioactive decay energy deposited by the positrons becomes significant, and before this models with locally trapped or free-streaming positrons are indistinguishable. Comparing the optimal model (12C) and model 12B, which differs only in the positron trapping, the bolometric corrections for the optimal model gets increasingly larger after ∼300 days, when the contribution from positrons to the energy deposition starts to become significant. The reason for this is that in the optimal model all positrons are trapped in the Fe/Co/He zone, and do not contribute to the heating of other zones. The Fe/Co/He zone has a lower temperature than other zones because of efficient cooling from the large number of iron lines, and the emission arising from this zone is redder. Not surprisingly, the effect on the U to z bolometric correction is strongest and begins earliest. The choice of local positron trapping for the optimal model (12C) is mainly motivated by the better fit to the pseudo-bolometric lightcurves after 300 days whereas the constraints obtained from nebular spectra (J14) are not conclusive.

4.1.5. Molecule emission

As discussed in Sect. 3.3.8 there is an excess in the 4.5 μm band, developing already during the first hundred days, but increasing dramatically between 100 and 250 days. The 4.5 μm band overlaps with both the CO fundamental band and the SiO first overtone band (see below) so molecule emission is a possible explanation. As also discussed in Sect. 3.3.8, we detect a modest amount of CO first overtone emission at 89 and 206 days, which implies at least some contribution from CO fundamental band emission to the 4.5 μm flux. Below we discuss how molecule cooling is treated in the J14 models, how it affects the lightcurves and which constraints could be obtained from comparisons with observations.

Molecule cooling only affects the way the deposited energy is processed (bolometric correction). It is included in the modelling in a simplified way, and is represented as the fraction of the deposited radioactive decay energy emitted as molecule (CO and SiO) emission in the O/C and O/Si/S zones. This energy is then emitted as CO and SiO fundamental and first overtone band emission, represented as box line profiles between 2.25-2.45 (CO first overtone), 4.4-4.9 (CO fundamental) and 4.0-4.5 (SiO first overtone) μm. The CO first overtone band overlaps with the K band and the CO fundamental and SiO first overtone bands with the 4.5 μm band whereas the SiO fundamental band lies outside the U to 4.5 μm wavelength range. The fundamental to first overtone band flux ratios are assumed to be the same as observed for CO in SN 1987A (Bouchet & Danziger 1993). We have used two configurations, one where the fraction of deposited radioactive decay energy emitted as molecule emission has been set to one, and one where this fraction has been set to zero. Comparing models 13D and 13F, which only differs in the amount of molecule cooling, the U to z and U to K bolometric corrections for model 13D (complete cooling) are 20-25 percent larger throughout the evolution. The U to 4.5 μm bolometric corrections, on the other hand, are similar. This reflects the fact the most of the molecule emission falls within the U to 4.5 μm wavelength range and the flux is mainly redistributed within this wavelength range. The effect of molecule cooling is very evident in the 4.5 μm lightcurve which is a factor of 100-10000 brighter for model 13D (complete cooling) as compared to model 13F (no cooling).

Molecule cooling is an important parameter in the modelling, not only because it affects the flux in the K and 4.5 μm bands. It also determines the fraction of the deposited radioactive decay energy available for line emission and the temperature in the O/C and O/Si/S zones. The observed CO first overtone emission at 89 and 206 days, implies some molecule cooling in the O/C zone. Models with complete molecule cooling overproduce the 4.5 μm flux with a factor of ∼10 whereas models without molecule cooling but with dust, as the optimal model, underproduce it with a factor of ∼10. Models without both molecule cooling and dust underproduce the 4.5 μm flux with a factor of 100-1000 and seem to be excluded. The strong similarity of the [O I] 6300 and Mg I] 4571 Å line profiles suggests the contribution from the O/C and O/Si/S zones to the [O I] 6300 Å emission to be modest, in turn suggesting the amount of molecule cooling in these zones to be significant. The redshift of the Ca II 8662 Å lines suggests a significant contribution from the [C I] 8727 Å line, found to arise mainly !is this correct! from the O/C zone in J14, in turn suggesting the amount of molecule cooling in the O/C zone to be modest. We have chosen no molecule cooling for our optimal model, but in the O/C zone an intermediate amount of cooling seems to be more likely.

4.1.6. Dust absorption and emission

As discussed in Sect. 3.2 there is a strong increase in the fractional MIR luminosity between 100 and 250 days during which an increase in the decline rate of the U to K pseudo-bolometric lightcurve is also observed. The increase in the decline rate is even more pronounced in the U to z pseudo-bolometric lightcurve (Fig. 17) and the increase in fractional luminosity affects both MIR bands as well as the K band (Fig. 8). This suggests that some process is re-distributing flux from the optical to the MIR during this period. One example of such a process is formation of dust in the ejecta, which would absorb the still quite hot radiation from the SN and re-emit it at a much lower temperature. Below we discuss how dust emission/absorption is treated

in the J14 models, how it affects the lightcurves and which constraints could be obtained from comparisons with observations.

Dust emission/absorption only affects the way the deposited energy is processed (bolometric correction). It is included in the modelling in a simplified way, and is represented as a gray absorptive opacity in the core zones. The absorbed luminosity is re-emitted as blackbody emission from a homologously expanding surface, representing a number of optically thick dust clouds. The fractional area of this surface x_{dust}, as compared to the area of the core, is a free parameter in the modelling, and determines the temperature of the emitted blackbody radiation. Comparing the optimal model (12C), for which dust has been added from 200 days and onwards, to model 12D the U to z bolometric correction for the former increases with ∼20 percent at 200 days, roughly corresponding to the optical depth of the added dust (see below). The U to K bolometric correction is marginally affected at 200 days but then slowly increases whereas the U to 4.5 μm bolometric correction is unaffected until ∼350 days and then slowly increases, both of which reflects the decreasing temperature of the dust (see below). The effect of dust (emission) is very evident in the K and the MIR lightcurves which increase with factor of a ∼10 and ∼100, respectively, at 200 days and then slowly evolve according to the decreasing temperature.

Using our simplified dust model, we find a value of 0.25 for the optical depth of the dust to match the behaviour of the U to z pseudo-bolometric lightcurve. The value of x_{dust} was derived by minimization of the sum of squares of the relative flux differences of model and observed K, 3.6 and 4.5 μm photometry at 200, 300, 400 and 500 days (excluding K when the NIR coverage ends). This gives a value of x_{dust} of 0.01, which corresponds to temperatures of 2000, 1100, 666 and 416 K at 200, 300, 400 and 500 days respectively. However, assuming a large number of dust clouds and a small filling factor, it is possible to show from the assumptions made that $\tau = 3/4x_{dust}$, so this value of x_{dust} is not consistent with our assumptions. Furthermore, as seen in Fig. 19, the MIR lightcurves are not well reproduced by the optimal model (12C), although the discrepancy is much worse for the same model without dust (12D). The discrepancy in the 4.5 μm band could be explained by additional flux from molecule emission, but the discrepancy in the 3.6 μm band can not. On the other hand, the optimal model (12C) gives a good fit to the U to z pseudo-bolometric lightcurve and does improve the discrepancy in the MIR considerably as compared to the same model without dust (12D).

As a further complication there might also be a contribution from heated CSM dust to the MIR emission. Helou et al. (2013) show that such a model could explain the early evolution, whereas they fail to reproduce the late evolution. It is possible that a combination of emission from ejecta dust, CSM dust and molecules could well explain the MIR evolution. Comparing model 12D, which has neither dust absorption/emission nor molecule cooling, to observations, there is a huge discrepancy in the MIR bands but also a considerable discrepancy in the K band. This strongly suggest that at least one and probably a number of these processes are contributing. However, as the observational constraints are limited, it is not clear how to disentangle the contributions from each other.

!We probably need to add an discussion of the abscence of blue-shifted line peaks at late times here!

4.2. Hydrodynamical modelling of the 0-100 days bolometric lightcurve

In B12 we presented a hydrodynamical model for SN 2011dh that well reproduced the observed 0-100 days bolometric lightcurve and photospheric velocity evolution. Here we use the grid of SN models constructed with HYDE and MESA STAR presented in E14b and the procedure described therein to fit the 0-100 days UV to MIR pseudo-bolometric lightcurves and photospheric velocities of SNe 2011dh, 1993J and 2008ax. The UV to MIR bolometric correction was assumed to be negligible, as is supported by the results in Sect. 4.1. The strength of the method as compared to previous hydrodynamical modelling is the ability to determine the errors in the model parameters arising from the observed quantities and the degeneracy of the solutions, issues previously discussed in E14a from approximate considerations. The progenitor and SN parameters are the helium core mass (M_{He}), the explosion energy (E), the mass of ejected ^{56}Ni (M_{Ni}) and the distribution of it (Mix_{Ni}). The stellar models consists of bare helium cores without a hydrogen envelope and, as discussed in E14b, this is sufficient to determine the explosion energy, helium core mass and mass and distribution of the ejected ^{56}Ni. As described in E14b equal weight is given to the diffusion phase lightcurve, the early tail lightcurve and the early photospheric velocity evolution. To estimate the radius, as we did in B12, modelling of the early cooling phase, which depends on the hydrogen envelope, is necessary. The UV to MIR pseudo-bolometric lightcurves for SNe 1993J and 2008ax were constructed by assuming the same UV and MIR fractions as for SN 2011dh.

Figure 22 shows the model bolometric lightcurve and photospheric velocity evolution compared to the observed UV to MIR pseudo-bolometric lightcurve and velocity evolution for the absorption minimum of the Fe II 5169 Å line for the optimal models of SNe 2011dh, 2008ax and 1993J. Table 3 gives the helium core mass, explosion energy, mass of ejected ^{56}Ni and the distribution of it for the optimal models and the corresponding errors, calculated as described in E14b. A systematic error of 15 percent in the photospheric velocities has been assumed. The derived parameters for SN 2011dh are in good agreement with the results in B12. The helium core mass and explosion energy derived for SNe 1993J and 2008ax are similar to what is derived for SN 2011dh, whereas the mass of ejected ^{56}Ni differs significantly. The mixing of the ^{56}Ni is strong for all three SNe and for SN 2011dh the fraction of ^{56}Ni outside 3500 and 6000 km s^{-1} is 53 and 8 percent respectively. This is in rough agreement with the optimal steady-state NLTE model, although in this model the ^{56}Ni is confined within 6000 km s^{-1}. We note that the velocity evolution of SN 2008ax is not well fitted, which could be explained by a worse correspondence between the absorption minimum of Fe II 5169 Å and the photosphere as compared to SNe 2011dh and 1993J.

In E14b we discuss the constraints on the model parameters obtained from the lightcurve and photospheric velocity evolution and the deneracy of the solution. In E14a we claimed that the diffusion and tail phase lightcurve provide independent constraints and that it might be possible to determine the model parameters from the lightcurve alone. This is true for a model with constant opacity like Arnett (1982) but in the hydrodynamical models the lightcurve provides the single constraint M_{ej}^2/E=const and the ejecta mass and explosion energy are degenerate. The photospheric velocity evolution, which provides the constraint M_{ej}/E=const, allows the degeneracy in ejecta mass and explosion energy to be broken and is essential to determine these

Table 3. Helium core mass, explosion energy, mass of the ejected ^{56}Ni and the distribution of it for the optimal models of SNe 2011dh, 1993J and 2008ax.

SN	E (10^{51} erg)	M_{He} ($M_\odot$)	M_{Ni} ($M_\odot$)	Mix_{Ni}
2011dh	0.55 (+0.40,-0.15)	3.44 (+0.70,-0.26)	0.075 (+0.028,-0.020)	1.10 (+0.06,-0.00)
2008ax	0.70 (+0.50,-0.30)	3.19 (+0.56,-0.39)	0.175 (+0.087,-0.099)	0.93 (+0.04,-0.00)
1993J	0.60 (+0.45,-0.20)	3.31 (+0.60,-0.25)	0.106 (+0.034,-0.028)	0.90 (+0.24,-0.08)

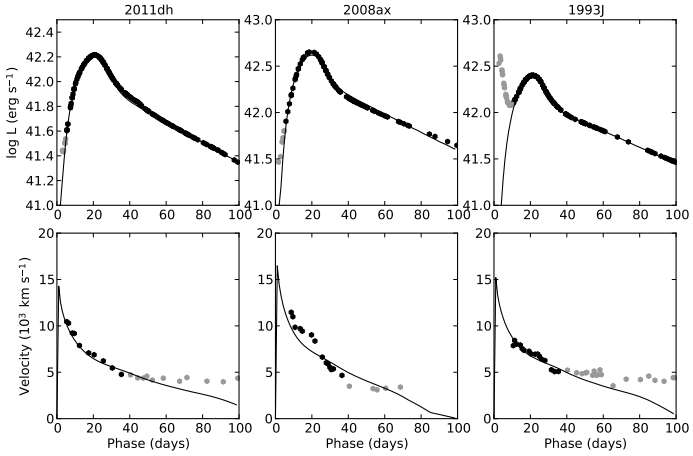

Fig. 22. Bolometric lightcurve (upper panels) and photospheric velocity evolution (lower panels) for the optimal models as compared to the observed UV to MIR pseudo-bolometric lightcurve and velocity evolution for the absorption minimum of the Fe II 5169 Å line for SNe 2011dh (left panels), 2008ax (middle panels) and 1993J (right panels). Observations not included in the fit are displayed in gray.

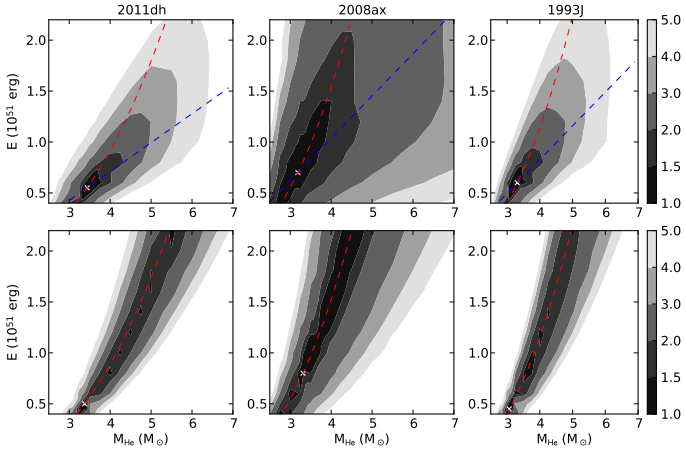

Fig. 23. Contour plots showing the standard deviation in the fits, normalized to that of the optimal model, projected onto the E-M_{He} plane for the case where the photospheric velocities were used (upper panels) and not used (lower panels) for SNe 2011dh (left panels), 2008ax (middle panels) and 1993J (right panels). We also show the constraints M_{ej}/E=const (blue) and M_{ej}^2/E=const (red) provided by the photospheric velocity evolution and the bolometric lightcurve, respectively.

parameters. This is well illustrated by Fig. 23 where we show contour plots of the standard deviation in the fit, normalized to that of the optimal model, as a function of helium core mass and explosion energy. Apparently there is an almost complete degeneray in the helium core mass and explosion energy along the M_{ej}^2/E=const curve if the fitting is done using the bolometric lightcurve alone. When the photospheric velocity evolution is used this degeneracy disappears and the fit becomes quite robust. If we assume a good fit to correspond to a normalized standard deviation of <2 and also take into account the errors arising from the observed quantities (Table 3) we find an upper limit on the helium core mass for all three SNe of $\lesssim$4 $M_\odot$, corresponding to an upper limit on the initial mass of $\lesssim$15 $M_\odot$.

4.3. Hydrodynamical modelling of the 0-300 days bolometric lightcurve

Here we extend the temporal coverage of the hydrodynamical model grid to 300 days (which is the period for which we have full U to 4.5 μm coverage), and make a fit of the observed U to 4.5 μm pseudo-bolometric lightcurve of SN 2011dh to this extended model grid. The 100-300 days bolometric lightcurves are calculated using HYDE whereas the 100-300 days U to 4.5 μm bolometric corrections are determined with the steady-state NLTE code. As in Sect. 4.2 we assume the bolometric correction to be negligible during the 0-100 days period. The fitting is done by minimization of the square of the relative residuals, giving equal weight to the diffusion phase lightcurve, the early tail lightcurve, the late tail lightcurve and the early photospheric velocity evolution This weighting scheme gives less weight to the photospheric velocities, which makes some sense as we have additional information about the lightcurve.

To use the method we need to know how the bolometric correction varies in the parameter space of the hydrodynamical grid. Calculating the bolometric correction for all hydrodynamical models with the steady-state NLTE code is not computationally feasible so we have to seek another solution. We take advantage of the fact that the U to 4.5 μm bolometric correction varies within ~0.05 mag between the J14 steady-state NLTE models during the 100-300 days period (Sect.4.1), and use the correction for the optimal steady-state NLTE model for all hydrodynamical models. However, as the J14 models cover a restricted volume of parameter space we need to justify this choice further. It is reasonable to assume that the bolometric correction depends mainly on the energy deposition per unit mass (determining the heating rate) and the density (determining the cooling rate). Furthermore, we know beforehand, that models giving a bad 0-100 days fit will not give a good 0-300 days fit. In Fig. 24 we have plotted the mass averaged density and the energy deposition per mass calculated as L_{Bol}/M_{ej} at 200 days for the J14 models and the hydrodynamical models with a normalized standard devia-

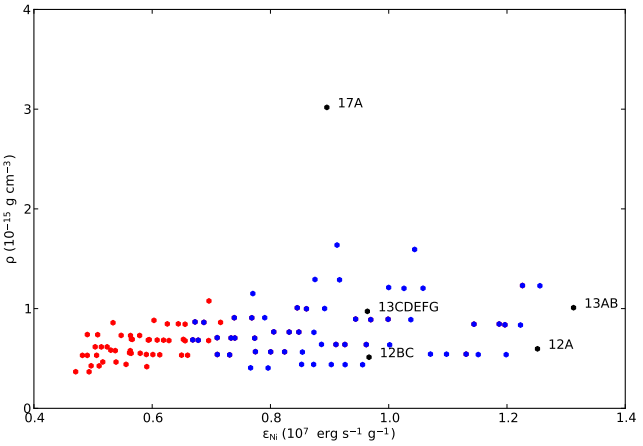

Fig. 24. Mass averaged density and energy deposition per mass calculated as L_{Bol}/M_{ej} at 200 days for the J14 models (black circles) and the hydrodynamical models with a normalized standard deviation in the 0-100 days fit less than 3 for the case where the photospheric velocities where used (blue circles) and not used (red circles).

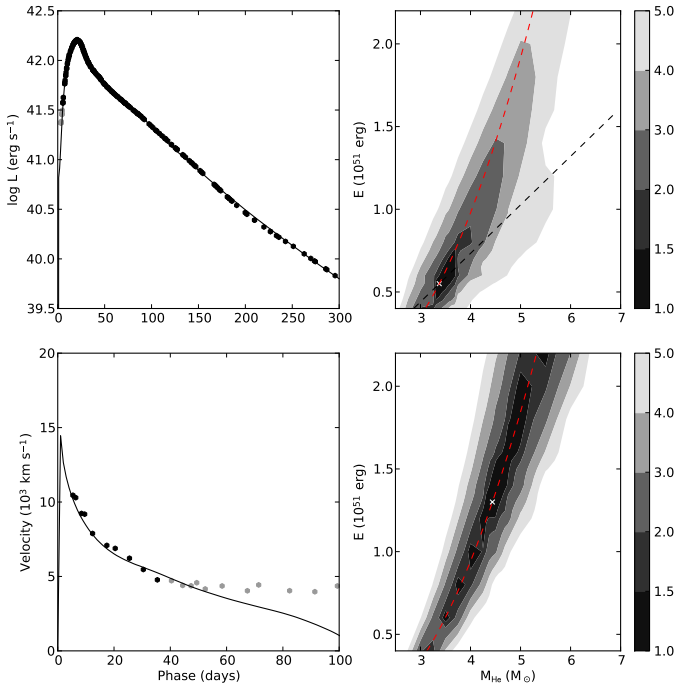

Fig. 25. Right panels: U to 4.5 μm pseudo-bolometric lightcurve (upper right panel) and photospheric velocity evolution (lower right panel) for the optimal model as compared to the observed U to 4.5 μm pseudo-bolometric lightcurve and velocity evolution for the absorption minimum of the Fe II 5169 Å line. Observations not included in the fit are displayed in grey. Left panels: Contour plots showing the standard deviation in the fit, normalized to that of the optimal model, projected onto the E-M_{He} plane for the case where the photospheric velocities were used (upper left panel) and not used (lower left panel). We also show the constraints M_{ej}/E=const (blue) and M_{ej}^2/E=const (red) provided by the photospheric velocity evolution and the bolometric lightcurve, respectively.

tion in the 0-100 days fit less than 3. It is clear from this figure that the hydrodynamical models that could possibly give a good fit do not span a wide range in density or energy deposition per mass and that the NLTE models cover about half of this region. Therefore the use of the U to 4.5 μm bolometric correction from the optimal steady-state NLTE model seems justified.

We also need to know that the steady-state NLTE model parameters that do not map onto the hydrodynamical model grid do not appreciably affect the bolometric lightcurve and the bolometric correction. A scan of parameter space with the steady-state NLTE code is not computationally feasible but the small differences in the U to 4.5 μm bolometric correction for the J14 models during the 100-300 days period make this caveat less worrying. The reason for this is that molecule cooling and dust emission/absorption mainly redistributes the flux within the U to 4.5 μm wavelength range, the dependence on the filling factors is weak and the fraction of the energy deposited by the positrons is low (Sect. 4.1). Molecule cooling and dust emission/absorption do not affect the bolometric lightcurve whereas the filling factors and the positron trapping do not affect the bolometric lightcurve for the J14 models but might otherwise do depending on the optical depths for γ-rays and positrons (Sect. 4.1). As the hydrodynamical models that could possibly give a good fit do not span a wide range in density, with respect to the bolometric lightcurve, the choice not to vary these steady-state NLTE-parameters seems justified.

Figure 25 shows the model U to 4.5 μm pseudo-bolometric lightcurve and photospheric velocity evolution compared to the observed U to 4.5 μm pseudo-bolometric lightcurve and velocity evolution for the absorption minimum of the Fe II 5169 Å line for the optimal model. The parameters of the optimal model are $E=0.55^{+0.40}_{-0.15}\times10^{51}$ erg, $M_{He}=3.38^{+0.58}_{-0.27}$ $M_\odot$, $M_{Ni}=0.075^{+0.028}_{-0.017}$ $M_\odot$ and $Mix_{Ni}=1.00^{+0.00}_{-0.00}$, in close agreement with the results from the 0-100 days bolometric lightcurve. Figure 25 also shows contour plots of the standard deviation in the fit, normalized to that of the optimal model, as a function of helium core mass and explosion energy. The solution is slighty better constrained in helium core mass and slightly worse constrained in explosion energy, which probably just releflects the less weight given to the photospheric velocities. As expected, the fit using the lightcurve alone is still completely degenerate in helium core mass and explosion energy along the M_{ej}^2/E=const curve. In the end, the main achivement is to prove that we get a good fit and similar best fit values using the 0-300 days U to 4.5 μm pseudo-bolometric lightcurve.

4.4. Time dependent effects and the 500-750 days bolometric lightcurve

Figure 26 shows the observed U to 4.5 μm and U to z pseudo-bolometric lightcurves compared to the bolometric lightcurve, deposited ^{56}Co γ-ray and positron luminosity and deposited ^{57}Co luminosity for the optimal steady-state NLTE model. The optimal hydrodynamical model produces very similar results. It is evident from the figure, that the deposited ^{56}Co luminosity is dominated by the positron contribution after ~450 day, and that the observed 500-750 days pseudo-bolometric lightcurves are unlikely to be powered by the γ-rays emitted in the ^{56}Co decay. Shivvers et al. (2013) suggested that the SN has entered a phase powered by the positrons emitted in the ^{56}Co decay after 300-350 days. Given our results, this suggestion seems to be roughly correct in the sense that the positron contribution dominates the deposited luminosity after ~450 days. However, as we will discuss below, it is not clear that the positron contribution dominates the emitted luminosity, because there is a number of processes that could provide additional energy sources.

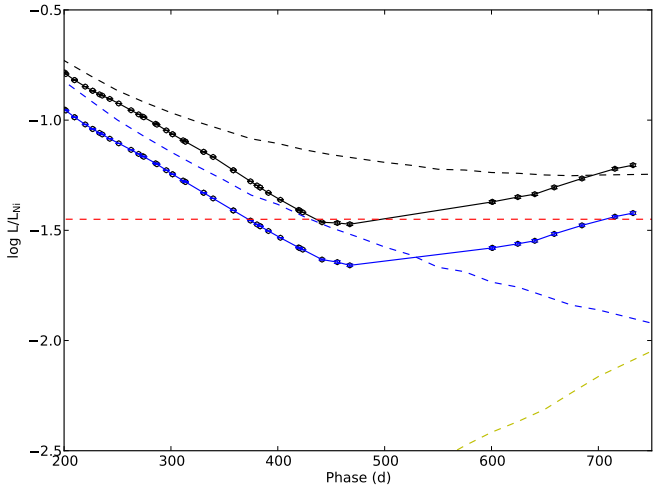

Fig. 26. U to 4.5 μm (black dots) and U to z (blue dots) pseudo-bolometric lightcurves compared to the bolometric lightcurve (black dashed line), deposited ^{56}Co decay gamma-ray (blue dashed line) and positron (red dashed line) luminosity and deposited ^{57}Co decay luminosity (yellow dashed line) for the optimal steady-state NLTE model (12C). The lightcurves have been normalized to the radioactive decay chain luminosity of 0.075 $M_\odot$ of ^{56}Ni.

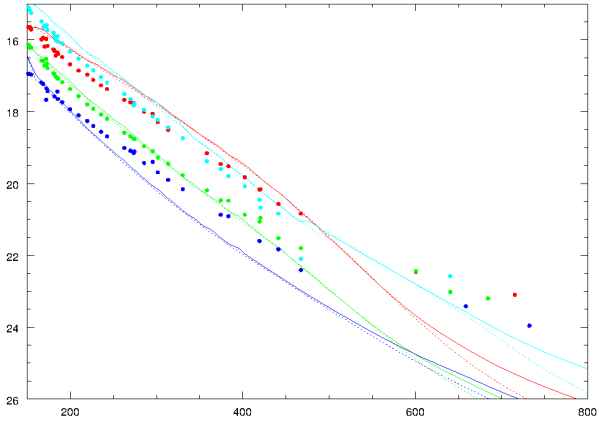

Fig. 27. Synthetic B (blue), V (yellow), r (red) and I (cyan) magnitudes for the optimal steady-state NLTE model (12C) as calculated with the time dependent NLTE code with (dashed lines) and without (solid lines) a steady-state assumption compared to the observed magnitudes (dots). !This figure has to be remade and does not show model 12C (but a similar model)!

There is observational evidence for additional energy sources from the observed pseudo-bolometric lightcurves. The decline rates of the pseudo-bolometric lightcurves between 500 and 750 days is 0.0065-0.0070 mag s^{-1}, significantly lower than the decay rate of ^{56}Co. As discussed in Sect. 4.1, the optimal steady-state NLTE model requires the positrons to be locally trapped to fit the 300-500 days U to z pseudo-bolometric lightcurve. This implies an increasing contribution from the low temperature Fe/Co/He zone (Sect. 4.1), in turn implying an increasing bolometric correction. However, the ratio of the observed U to z pseudo-bolometric luminosity and the bolometric luminosity of the optimal steady-state NLTE model, increases from ∼0.3 to ∼0.5 between 450 and 750 days, in contradiction with this expectation.

If the recombination time scales become longer than the time scale of the ^{56}Co decay, the steady-state assumption required for the NLTE modelling is no longer valid. Some fraction of the deposited radioactive decay energy will then build up a reservoir of ionization energy, which through recombination emission could eventually dominate the emitted luminosity. This process is called freeze-out and, as discussed in J14, approximate calculations suggest that in the hydrogen-rich envelope freeze-out occurs already at 100-200 days and in the helium envelope at ∼500 days !is this correct!. The contribution from the hydrogen envelope, which absorbs a negligible fraction of the radioactive decay energy, is likely to be small whereas the contribution from the helium envelope could very well be substantial. We use a time-dependent NLTE code (Kozma & Fransson 1992, 1998a,b) to test the steady-state assumption for our optimal steady-state NLTE model. Figure 27 shows the synthetic B, V, r and I band photometry, with and without a steady-state assumption, as modelled with this code. It is clear from the figure, that time-dependent effects start to become important at ∼600 days, and after ∼700 days recombination emission from the helium envelope provides a dominant and increasing contribution to the flux in these bands. To determine if the additional energy source provided by freeze-out in the helium envelope can fully explain the late-time evolution of the pseudo-bolometric lightcurves is outside the scope of this paper, but it is clear that this contribution is likely to be substantial. The 678 day spectrum of SN 2011dh presented by Shivvers et al. (2013) !Is this date correct, there is 2 spectra!, shows features not present in our last optical spectra that could be identified as the He I 6678 Å and 7065 Å lines, whereas the strong feature identified as Na I 5890,5896 Å by the authors could have a significant contribution from, or be fed by, the He I 5876 Å line. This is consistent with a substantial contribution from helium envelope recombination emission at this epoch.

CSM interaction became the dominant energy source at ∼300 days for SN 1993J !reference!, giving rise to broad box-like Hα and Na I 5890,5896 Å lines and a considerable flattening of the lightcurves. The 678 day spectrum of SN 2011dh presented by Shivvers et al. (2013) !Is this date correct, there is 2 spectra! shows a feature that is interpreted as broad box-like Hα emission by the authors, but no broad box-like Na I 5890,5896 Å emission is seen. The interpretation of the broad feature as Hα emission is far from clear, as a number of other lines may contribute in this wavelength range (including the He I 6678 Å line discussed above), and the feature is also much weaker than for SN 1993J at a similar epoch. Additional energy sources could also be provided by the decay of radioactive isotopes other than ^{56}Co. In the optimal steady-state NLTE model, the fractional luminosity deposited by the ^{57}Co decay is ∼10 percent at 700 days and increasing. A higher mass of ejected ^{57}Co than assumed in the optimal steady-state NLTE model, can not be excluded, and could help explain the observed evolution.

In summary we find observational and theoretical evidence that the contribution from positrons emitted in the ^{56}Co decay does not dominate the late-time luminosity. We find a substantial contribution from recombination emission in the helium envelope due to freeze-out likely and substantial contributions from CSM interaction and other radioactive isotopes less likely.

5. Discussion

5.1. The nature of the progenitor star

In M11, B12, E14a, J14 and this paper we investigate the nature of the progenitor star using a number of different and, at least partially, independent methods. In M11 we analyse direct observations of the star by comparison of the observed magnitudes to predictions from stellar atmosphere and evolutionary models. The best match is found to be a yellow supergiant with an initial mass of 13±3 $M_\odot$ and a radius of ∼270 $R_\odot$. In E14a we present observations of the disappearance of this star, thus confirming that it was the progenitor of SN 2011dh. In this paper we present hydrodynamical modelling, which shows that a star with a helium core mass of $3.3^{+0.6}_{-0.2}$ $M_\odot$, exploded with and energy of $0.50^{+0.42}_{-0.10}\times10^{51}$ erg and ejecting $0.075^{+0.028}_{-0.013}$ $M_\odot$ of ^{56}Ni mixed out to high velocities, gives the best fit to the observed 3-300 days bolometric lightcurve and the photospheric velocity evolution. The use of a model grid allows us to determine the errors in the SN and progenitor parameters arising from the errors in the observed quantities and to constrain the degeneracy of the solution. Given this we find an upper limit on the initial mass of $\lesssim$15 $M_\odot$. In B12 we present hydrodynamical modelling, which shows that a low-mass (∼0.1 $M_\odot$) and extended (200-300 $R_\odot$) hydrogen-rich envelope seems to be required to reproduce the observed *g* band lightcurve during the first 3 days. In E14a we estimate a hydrogen mass of 0.01-0.04 $M_\odot$ using a Monte-Carlo atmosphere code. This hydrogen mass is consistent with the B12 ejecta model, and we also find the interface between the helium core and the hydrogen rich envelope to be located at a velocity consistent with this model. In J14 and this paper we present steady-state NLTE modelling, which shows that a star with an initial mass of 12 $M_\odot$ well reproduces the observed 100-500 days spectral evolution and pseudo-bolometric and photometric lightcurves. The evolution in the MIR however, which is complex and depends on both dust and molecule (CO and SiO) emission, is not well reproduced. Particular attention is paid to the [O I] 6300,6364 Å line, which is very sensitive to the initial mass of the star. To reproduce the flux in this line an initial mass of <17$M_\odot$ seems to be required. After 500 days modelling using a time-dependent NLTE code (Kozma & Fransson 1992, 1998a,b), shows that freeze-out in the helium envelope becomes important and the assumption of steady-state is no longer valid.

Overall the results obtained with the different methods are consistent and, even given the caveats of each individual method, it is likely that the progenitor star is of moderate initial mass ($\lesssim$15 $M_\odot$), and has a low-mass extended hydrogen rich envelope, most of which must have been lost either through stellar winds or interaction with a binary companion. The moderate mass suggests that interaction with a binary companion is needed, as stellar winds of stars in this mass range are not strong enough to expel the hydrogen envelope before core-collapse. As we show in J14 and in this paper, using steady-state NLTE modelling of nebular spectra and hydrodynamical modelling of the bolometric lightcurves, SNe 2008ax and 1993J are likely to be of similar initial mass and have similar explosion energy as SN 2011dh, although the mass of the ejected ^{56}Ni may differ significantly depending on the adopted distance and extinction. In particular, the upper bound on the initial mass for all three SNe is found to be $\lesssim$15 $M_\odot$. For the same reason as discussed above, this suggests that interaction with a binary companion have taken place. In the case of SN 1993J, this conclusion is supported by direct observations of the binary companion (Maund et al. 2004). Observations, that could detect or set useful constraints on the presence of a companion star for SN 2011dh, are scheduled for Cycle 21 at HST, whereas similar observations for SN 2008ax would not be feasible, due to the longer distance. Clearly there is growing evidence that the main production channel for Type IIb SNe are stars whose hydrogen envelope has been stripped by interaction with a binary companion. Modelling of the nebular spectra and hydrodynamical modelling of the bolometric lightcurves for a larger sample of Type IIb SNe, could provide further evidence for this hypothesis.

6. Conclusions

We present two years of optical and NIR photometric and spectroscopic observations for the Type IIb SN 2011dh. Together with SWIFT and Spitzer observations the data cover the UV to MIR wavelength range although the photometric coverage ends at ∼100 days in UV and at ∼350 days in NIR, and the spectral coverage ends at ∼200 days in NIR and at ∼450 days in the optical. Particular attention is paid to the bolometric and photometric lightcurves where we use steady-state NLTE modelling and hydrodynamical modelling to put constraints on the SN and progenitor parameters. We also provide a spectral analysis, mainly related to the line profiles, complementary to the steady-state NLTE modelling of nebular spectra presented in J14.

The 0-100 days UV to MIR pseudo-bolometric lightcurve and the photospheric velocities of SN 2011dh are analysed using the grid of the hydrodynamical SN models presented in E14b and the fitting procedure described therein. To extend the temporal coverage of the model grid to 300 days we apply a *U* to 4.5 μm bolometric correction determined with the steady-state NLTE modelling. The method used allows us to determine the errors in the model parameters arising from the observed quantities and the degeneracy of the solution. The results for the 0-300 days period are very similar to those for the 0-100 days period and we find a helium core mass of $3.4^{+0.6}_{-0.3}$ $M_\odot$, an explosion energy of $0.55^{+0.40}_{-0.16}\times10^{51}$ erg and a mass of ejected ^{56}Ni of $0.075^{+0.028}_{-0.017}$ $M_\odot$, in good agreement with our results in B12. The 0-100 days bolometric lightcurves and photospheric velocities of SNe 2008ax and 1993J are also analysed and the best fit values of the helium core mass and explosion energy are similar to those of SN 2011dh. We find an upper limit on the helium core mass for all three SNe of $\lesssim$4 $M_\odot$, corresponding to an upper limit on the initial mass of $\lesssim$15 $M_\odot$. Strong mixing of the ejected ^{56}Ni is required for all three SNe to fit the rise to peak luminosity.

The 100-500 days pseudo-bolometric and photometric lightcurves of SN 2011dh are analysed using the restricted set of steady-state NLTE models presented in J14. To extend the temporal coverage of these models we construct 0-100 days bolometric lightcurves using HYDE (E14b) in homologous mode. The optimal 12 $M_\odot$ model, presented in J14 and chosen to give the best agreement with both spectra and lightcurves, shows a good overall agreement with the observed pseudo-bolometric lightcurves. Local trapping of the positrons emitted in the ^{56}Co decay gives the best fit the 300-500 days *U* to *z* pseudo-bolometric lightcurve and the amounts of dust and molecule cooling are strongly related to the evolution in the MIR. As compared to models without dust and molecule cooling we find a huge excess in the MIR and a considerable excess in the *K* band developing between 100 and 250 days, during which an increase in the decline rates of the *U* to *z* and *U* to *K* pseudo-bolometric lightcurves is also observed. Models with a modest amount of dust (τ = 0.25) formed in the ejecta during this period reproduce this behaviour although the MIR fluxes are underproduced

by a factor of ∼10. CO first overtone band emission is detected in NIR spectroscopy at 89 and 202 days implying a contribution to the 4.5 μm band flux from CO fundamental band emission at these epochs. Neither complete molecule cooling nor absence of molecule cooling well reproduce the 4.5 μm magnitudes. In the C/O zone an intermediate amount of molecule cooling is supported by the observed CO first overtone emission and the similarity of the [O I] 6300 Å and Mg I] 4571 Å lines (see below).

The 500-750 days lightcurves are harder to analyse and modelling with a time-dependent NLTE code (Kozma & Fransson 1992, 1998a,b) shows that, in this phase, the steady-state assumption is no longer valid. In the optimal steady-state NLTE model the positron contribution dominates the ^{56}Co energy deposition after ∼450 days. However, there is both observational and theoretical evidence that the 500-750 days lightcurves are dominated by additional energy sources. The decline rates are significantly lower than the decay rate of ^{56}Co and the observed U to z pseudo-bolometric luminosity is ∼50 percent of the bolometric luminosity in our optimal model, in contradiction with a scenario with locally trapped positrons. Modelling with the time-dependent NLTE code shows that after ∼600 days freeze-out in the helium envelope becomes important, and recombination emission from the helium envelope is likely to contribute substantially to the observed luminosity. We find a substantial contribution from CSM interaction and other radioactive isotopes less likely.

The line profiles of the important lines are analysed and we estimate the sizes of the oxygen, magnesium, iron and [Ca II] 7291,7323 Å line emitting regions to 2900-3400, 2700-3600, 1600-2100 and 2100-2400 km s^{-1} respectively, in all compared cases smaller than those of SNe 1993J and 2008ax. Given the findings in J14, these regions would correspond to the oxygen, O/Ne/Mg, Fe/Co/He and Si/S nuclear burning zones and suggest partial mixing of the core material. The profiles of the [O I] 6300 Å and Mg I] 4571 Å lines show a remarkable similarity, suggesting that these lines arise from the same nuclear burning zone. Given the findings in J14, this would be the O/Ne/Mg zone and contributions from the O/Si/S and O/C zones to the [O I] 6300 Å flux would be modest, in turn suggesting the amount of molecule (CO and SiO) cooling in these zones to be considerable. We use repetitions of small scale fluctuations in the [O I] 6300 Å and [O I] 6364 Å lines to find a line ratio close to 3, consistent with optically thin emission and in agreement with the results in J14, from 200 days and onwards. Applying the method of Chugai (1994) to these small scale fluctuations, we find an upper limit on the filling factor of the [O I] 6300 Å and Mg I] 4571 Å line emitting material of ∼0.07 and a lower limit on the number of clumps of ∼900.

This paper concludes our observational and modelling work on SN 2011dh presented in M11, B12, E14a and J14. We have applied stellar evolutionary progenitor analysis, hydrodynamical modelling, SN atmosphere modelling and steady-state NLTE modelling to our extensive set of observational data. Although a number of issues remains unsolved, as the photometric evolution in the MIR and the late time flattening of the lightcurve, the main characteristics of the SN and its progenitor star found by the different methods are consistent. The progenitor star appears to have been of moderate (12-15 $M_\odot$) initial mass, and the 3-4 $M_\odot$ helium core surrounded by a low-mass (∼0.1 $M_\odot$) and extended (200-300 $R_\odot$) hydrogen-rich envelope. In particular we have found the initial masses of SNe 2011dh, 1993J and 2008ax to be $\lesssim$15 $M_\odot$, from both hydrodynamical modelling of the early bolometric evolution and steady-state NLTE modelling of the late spectral evolution. This limit is also supported by stellar evolutionary progenitor analysis for SNe 2011dh and 1993J (Maund et al. 2004, 2011). Given that the mass-loss rates for stars in this mass range are probably not strong enough to expell the hydrogen envelope before core-collapse, a binary origin for these SNe is strongly suggested.

7. Acknowledgements

References

Arnett, W. D. 1982, ApJ, 253, 785
Benvenuto, O. G., Bersten, M. C., & Nomoto, K. 2013, ApJ, 762, 74
Bersten, M. C., Benvenuto, O. G., Nomoto, K., et al. 2012, ApJ, 757, 31
Bouchet, P. & Danziger, I. J. 1993, A&A, 273, 451
Chugai, N. N. 1994, ApJ, 428, L17
Ergon, M., Jerkstrand, A., Bersten, M., Sollerman, J., & Fransson, C. 2014a, In preparation
Ergon, M., Sollerman, J., Fraser, M., et al. 2014b, A&A, 562, A17
Griga, T., Marulla, A., Grenier, A., et al. 2011, Central Bureau Electronic Telegrams, 2736, 1
Hammer, N. J., Janka, H.-T., & Müller, E. 2010, ApJ, 714, 1371
Helou, G., Kasliwal, M. M., Ofek, E. O., et al. 2013, ApJ, 778, L19
Jerkstrand, A., Ergon, M., Smartt, S., et al. 2014, In preparation
Jerkstrand, A., Fransson, C., & Kozma, C. 2011, A&A, 530, A45
Jerkstrand, A., Fransson, C., Maguire, K., et al. 2012, A&A, 546, A28
Kozma, C. & Fransson, C. 1992, ApJ, 390, 602
Kozma, C. & Fransson, C. 1998a, ApJ, 496, 946
Kozma, C. & Fransson, C. 1998b, ApJ, 497, 431
Matheson, T., Filippenko, A. V., Ho, L. C., Barth, A. J., & Leonard, D. C. 2000, AJ, 120, 1499
Maund, J. R., Fraser, M., Ergon, M., et al. 2011, ApJ, 739, L37
Maund, J. R., Smartt, S. J., Kudritzki, R. P., Podsiadlowski, P., & Gilmore, G. F. 2004, Nature, 427, 129
Milisavljevic, D., Fesen, R. A., Gerardy, C. L., Kirshner, R. P., & Challis, P. 2010, ApJ, 709, 1343
Podsiadlowski, P., Hsu, J. J. L., Joss, P. C., & Ross, R. R. 1993, Nature, 364, 509
Sahu, D. K., Anupama, G. C., & Chakradhari, N. K. 2013, MNRAS, 433, 2
Shivvers, I., Mazzali, P., Silverman, J. M., et al. 2013, ArXiv e-prints
Stancliffe, R. J. & Eldridge, J. J. 2009, MNRAS, 396, 1699
Stathakis, R. A., Dopita, M. A., Cannon, R. D., & Sadler, E. M. 1991, Supernovae, 649
Taubenberger, S., Navasardyan, H., Maurer, J. I., et al. 2011, MNRAS, 413, 2140
Taubenberger, S., Valenti, S., Benetti, S., et al. 2009, MNRAS, 397, 677
Tsvetkov, D. Y., Volkov, I. M., Baklanov, P., Blinnikov, S., & Tuchin, O. 2009, Peremennye Zvezdy, 29, 2
Tsvetkov, D. Y., Volkov, I. M., Sorokina, E., et al. 2012, Peremennye Zvezdy, 32, 6
Van Dyk, S. D., Li, W., Cenko, S. B., et al. 2011, ApJ, 741, L28
Van Dyk, S. D., Zheng, W., Clubb, K. I., et al. 2013, ApJ, 772, L32
Woosley, S. E. & Heger, A. 2007, Phys. Rep., 442, 269
Yaron, O. & Gal-Yam, A. 2012, PASP, 124, 668

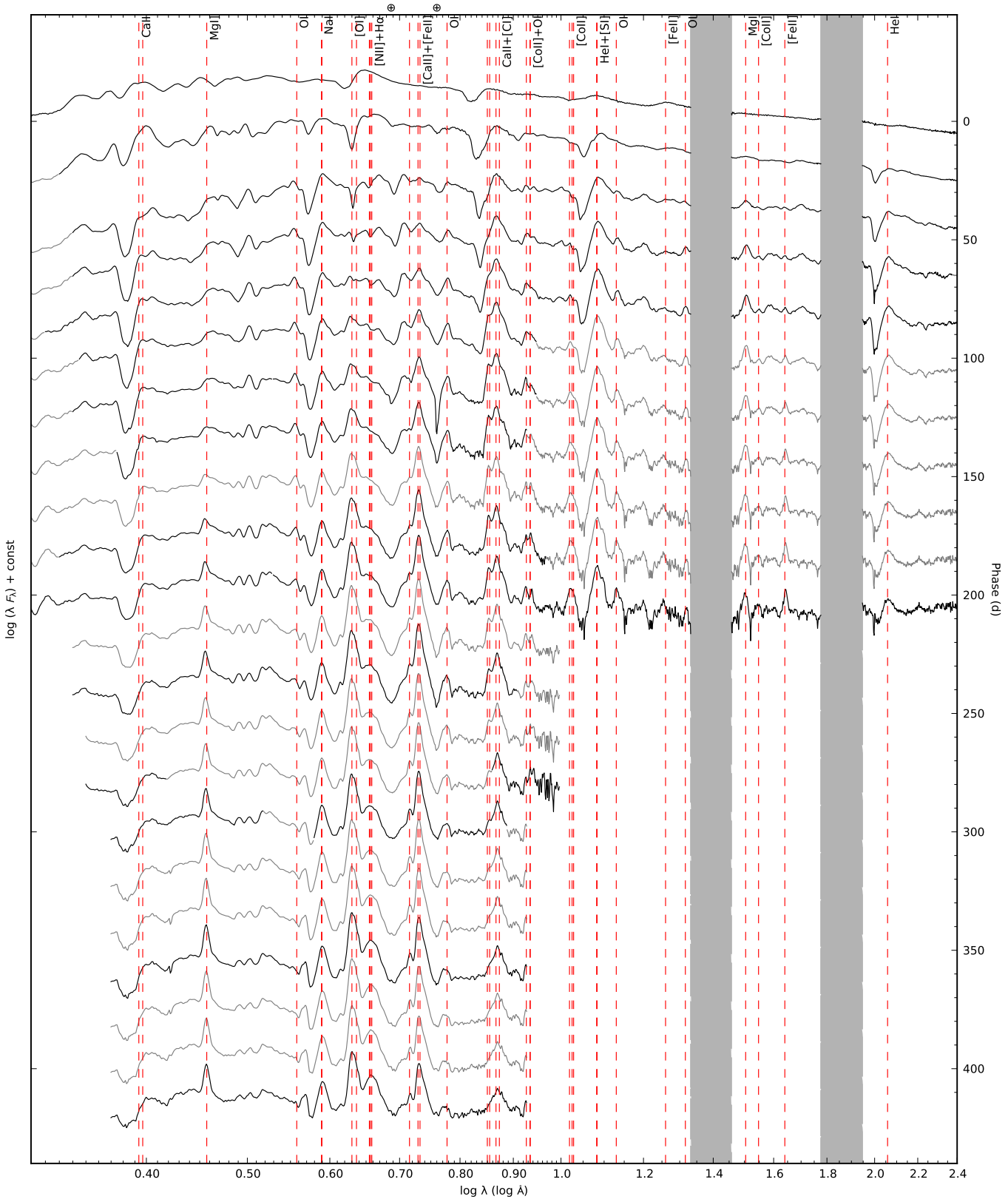

Fig. 2. Optical and NIR (interpolated) spectral evolution for SN 2011dh for days 5−425 with a 20-day sampling. Telluric absorption bands are marked with a ⊕ symbol in the optical and shown as grey regions in the NIR.

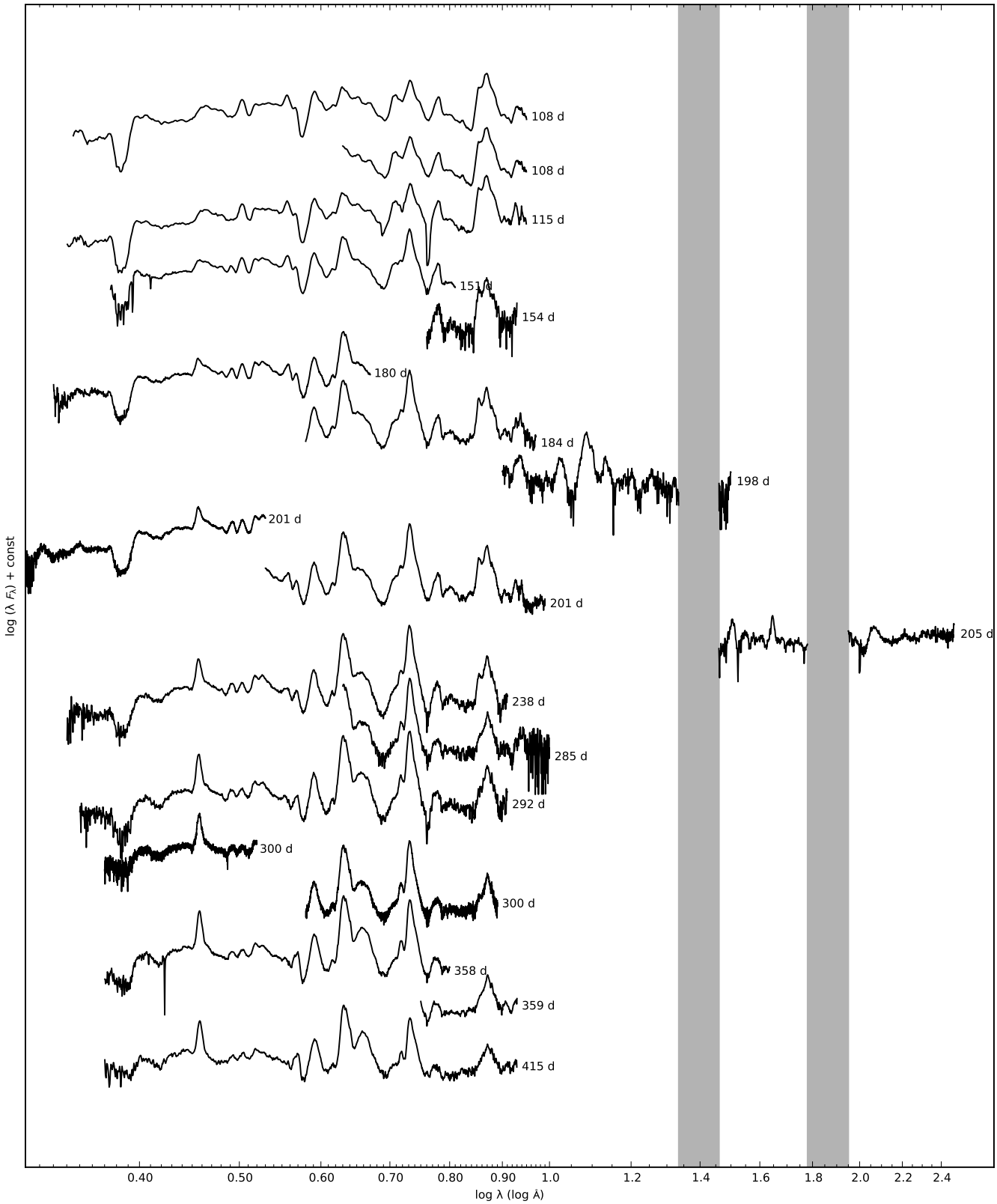

Fig. 3. Sequence of the observed late-time (100-415 days) spectra for SN 2011dh. Spectra obtained on the same night using the same telescope and instrument have been combined and each spectra have been labelled with the phase of the SN. Telluric absorption bands are marked with a ⊕ symbol in the optical and shown as grey regions in the NIR. !The AS-1.82/AFOSC spectra from 117 days is not yet included here.!

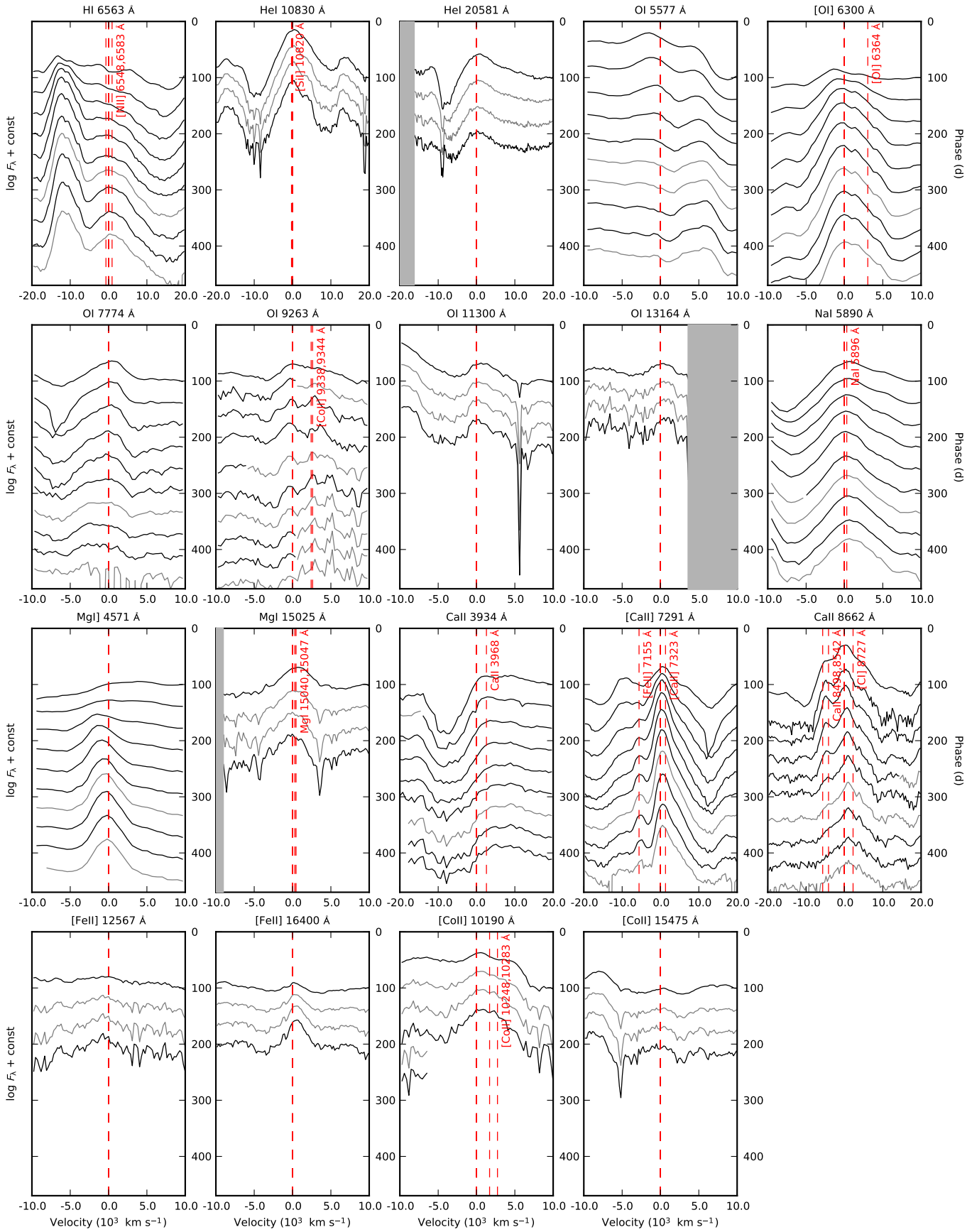

Fig. 9. Spectral evolution of all identified lines. Multiple or blended lines are marked with red dashed lines and telluric absorption bands in the NIR shown as grey regions.

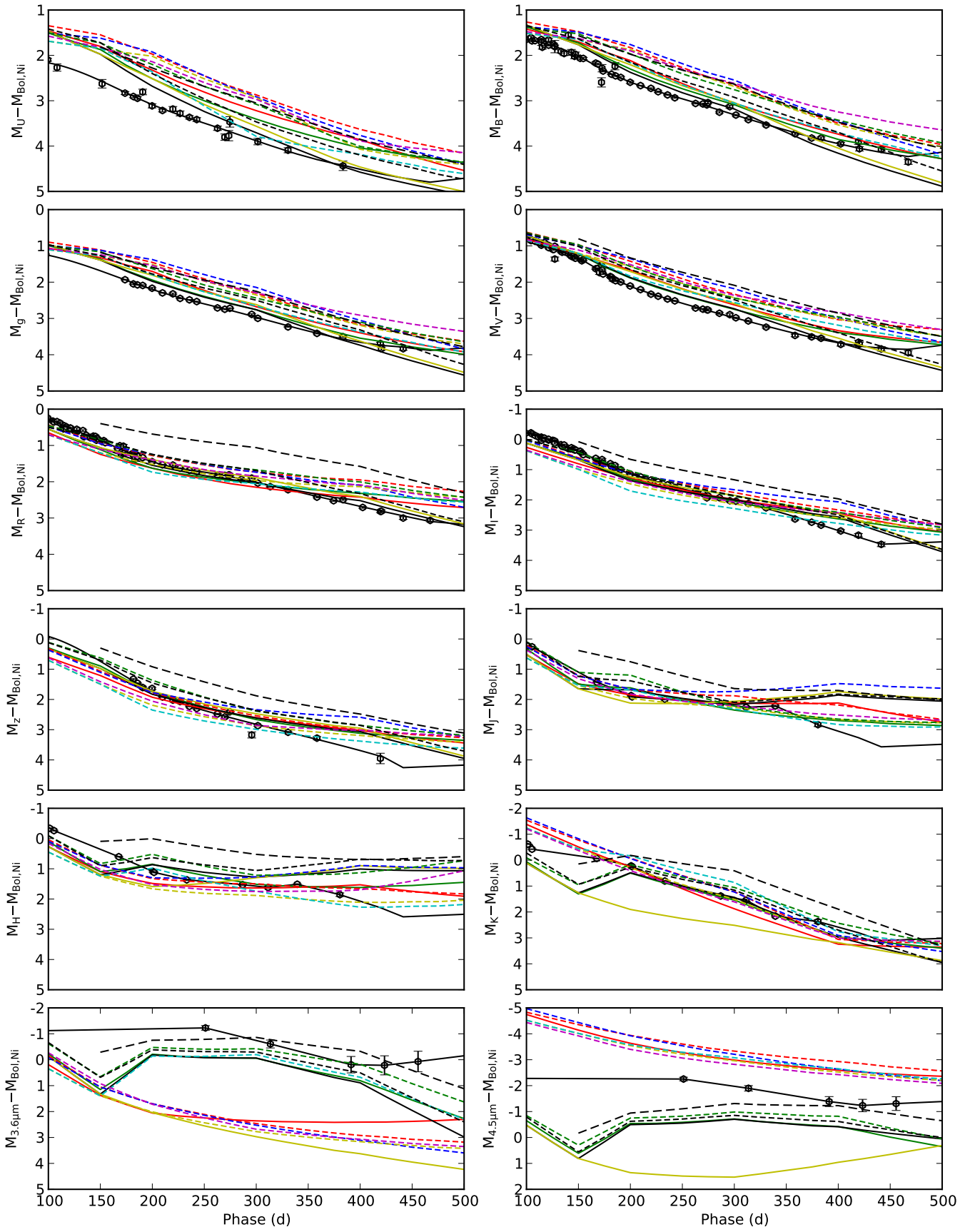

Fig. 19. 100-500 days Optical, NIR and MIR magnitudes for the J14 models as compared to the observed magnitudes. The lightcurves have been normalized to the radioactive decay chain luminosity of 0.075 $M_\odot$ of ^{56}Ni and the models are displayed as in Fig. 21.

Table 4. Optical colour-corrected JC *U* and S-corrected JC *BVRI* magnitudes for SN 2011dh. Errors are given in parentheses. For completeness data for the first 100 days already published in E14a are included. !One AFOSC observations from 2011-11-20 is not yet included in the table.!

JD (+2400000) (d)	Phase (d)	*U* (mag)	*B* (mag)	*V* (mag)	*R* (mag)	*I* (mag)	Telescope (Instrument)
55716.43	3.43	14.99 (0.03)	15.35 (0.02)	14.92 (0.02)	14.54 (0.01)	14.41 (0.02)	LT (RATCam)
55716.43	3.43	15.15 (0.08)	15.39 (0.02)	14.94 (0.02)	14.57 (0.01)	14.46 (0.01)	TNG (LRS)
55717.43	4.43	15.03 (0.03)	15.14 (0.02)	14.67 (0.03)	14.25 (0.01)	14.26 (0.03)	LT (RATCam)
55717.48	4.48	15.17 (0.09)	15.21 (0.03)	14.63 (0.03)	14.24 (0.01)	14.23 (0.02)	AS-1.82m (AFOSC)
55717.48	4.48	...	15.12 (0.03)	14.63 (0.02)	14.27 (0.01)	14.28 (0.02)	CANTAB (BIGST8)
55718.48	5.48	...	14.84 (0.01)	14.28 (0.02)	13.94 (0.01)	13.94 (0.01)	LT (RATCam)
55718.57	5.57	14.68 (0.06)	14.84 (0.02)	14.24 (0.02)	13.91 (0.01)	14.04 (0.01)	CA-2.2m (CAFOS)
55720.42	7.42	14.42 (0.02)	14.25 (0.01)	13.75 (0.03)	13.41 (0.01)	13.43 (0.02)	LT (RATCam)
55721.42	8.42	14.28 (0.10)	14.02 (0.01)	13.48 (0.01)	13.22 (0.01)	13.24 (0.02)	LT (RATCam)
55721.43	8.43	14.07 (0.07)	14.06 (0.01)	13.60 (0.04)	13.27 (0.02)	13.34 (0.02)	NOT (ALFOSC)
55722.42	9.42	...	13.86 (0.01)	13.29 (0.01)	13.05 (0.01)	13.07 (0.01)	LT (RATCam)
55723.41	10.41	13.98 (0.06)	13.71 (0.01)	13.16 (0.01)	12.89 (0.01)	12.90 (0.01)	LT (RATCam)
55724.41	11.41	13.91 (0.08)	13.62 (0.01)	13.03 (0.01)	12.79 (0.01)	12.77 (0.01)	LT (RATCam)
55725.39	12.39	...	...	12.94 (0.02)	12.66 (0.01)	...	MONTCAB (BIGST8)
55725.43	12.43	13.88 (0.07)	13.52 (0.02)	12.92 (0.04)	12.68 (0.01)	12.68 (0.01)	LT (RATCam)
55726.36	13.36	...	13.52 (0.01)	12.91 (0.02)	12.59 (0.01)	...	MONTCAB (BIGST8)
55728.40	15.40	...	13.39 (0.01)	12.77 (0.01)	12.44 (0.01)	...	MONTCAB (BIGST8)
55729.39	16.39	13.65 (0.01)	13.35 (0.01)	12.77 (0.06)	12.39 (0.01)	12.35 (0.02)	LT (RATCam)
55730.40	17.40	13.64 (0.03)	13.33 (0.01)	12.66 (0.01)	12.36 (0.01)	12.32 (0.01)	LT (RATCam)
55731.41	18.41	13.74 (0.09)	13.30 (0.01)	12.60 (0.02)	12.31 (0.01)	12.27 (0.01)	LT (RATCam)
55731.82	18.82	...	...	...	12.33 (0.02)	12.25 (0.01)	FTN (FS02)
55732.40	19.40	...	13.35 (0.03)	12.61 (0.01)	12.27 (0.01)	12.21 (0.01)	CANTAB (BIGST8)
55732.41	19.41	13.44 (0.06)	13.36 (0.02)	12.64 (0.02)	12.33 (0.02)	12.31 (0.02)	NOT (ALFOSC)
55732.46	19.46	13.71 (0.07)	13.32 (0.01)	12.58 (0.01)	12.28 (0.02)	12.22 (0.01)	LT (RATCam)
55733.45	20.45	13.67 (0.07)	...	...	12.26 (0.01)	12.20 (0.02)	LT (RATCam)
55734.52	21.52	13.37 (0.05)	13.33 (0.01)	12.58 (0.01)	12.25 (0.01)	12.29 (0.01)	CA-2.2m (CAFOS)
55735.44	22.44	13.91 (0.04)	...	...	12.26 (0.01)	12.16 (0.01)	LT (RATCam)
55736.44	23.44	14.13 (0.08)	...	...	12.26 (0.01)	12.16 (0.01)	LT (RATCam)
55737.39	24.39	...	13.65 (0.01)	12.72 (0.01)	...	...	LT (RATCam)
55738.42	25.42	14.50 (0.04)	13.79 (0.02)	12.81 (0.01)	12.32 (0.02)	12.22 (0.01)	LT (RATCam)
55738.51	25.51	14.20 (0.04)	13.77 (0.02)	12.82 (0.01)	12.38 (0.01)	12.26 (0.01)	NOT (ALFOSC)
55739.43	26.43	14.73 (0.04)	13.95 (0.02)	12.88 (0.01)	12.38 (0.01)	12.23 (0.01)	LT (RATCam)
55740.36	27.36	...	14.09 (0.04)	12.93 (0.01)	12.45 (0.01)	12.29 (0.01)	MONTCAB (BIGST8)
55740.43	27.43	14.91 (0.03)	14.12 (0.01)	12.97 (0.01)	12.48 (0.01)	12.30 (0.01)	LT (RATCam)
55740.44	27.44	...	...	12.97 (0.01)	12.47 (0.01)	...	TJO (MEIA)
55741.44	28.44	...	...	...	12.54 (0.01)	12.32 (0.01)	LT (RATCam)
55742.49	29.49	15.33 (0.01)	...	...	12.62 (0.01)	12.40 (0.01)	LT (RATCam)
55743.41	30.41	...	14.53 (0.01)	13.27 (0.02)	...	...	LT (RATCam)
55743.42	30.42	15.18 (0.05)	14.51 (0.02)	...	12.65 (0.01)	12.53 (0.01)	CA-2.2m (CAFOS)
55743.42	30.42	15.43 (0.05)	14.53 (0.01)	13.26 (0.03)	12.68 (0.01)	12.49 (0.01)	NOT (ALFOSC)
55745.39	32.39	15.74 (0.03)	14.74 (0.01)	13.44 (0.01)	12.77 (0.01)	12.56 (0.01)	NOT (ALFOSC)
55745.44	32.44	15.93 (0.04)	...	...	12.81 (0.01)	12.53 (0.01)	LT (RATCam)
55745.80	32.80	...	...	...	12.80 (0.01)	12.51 (0.01)	FTN (FS02)
55746.45	33.45	16.07 (0.04)	14.87 (0.03)	13.51 (0.01)	12.83 (0.01)	12.55 (0.02)	LT (RATCam)
55747.44	34.44	16.12 (0.04)	...	...	12.89 (0.01)	12.59 (0.01)	LT (RATCam)
55748.43	35.43	16.02 (0.02)	14.97 (0.01)	13.62 (0.01)	12.88 (0.01)	12.65 (0.01)	NOT (ALFOSC)
55748.44	35.44	16.27 (0.04)	...	...	12.94 (0.01)	12.62 (0.01)	LT (RATCam)
55750.40	37.40	16.20 (0.04)	15.10 (0.01)	13.73 (0.01)	13.03 (0.01)	12.73 (0.01)	NOT (ALFOSC)
55750.42	37.42	16.41 (0.14)	15.11 (0.02)	13.78 (0.03)	13.03 (0.01)	12.73 (0.02)	LT (RATCam)
55751.41	38.41	...	15.14 (0.01)	13.81 (0.01)	13.08 (0.01)	12.73 (0.01)	TJO (MEIA)
55751.43	38.43	...	...	...	13.11 (0.01)	12.77 (0.01)	LT (RATCam)
55752.45	39.45	16.54 (0.16)	...	...	13.13 (0.01)	12.75 (0.01)	LT (RATCam)

Table 4. Continued.

JD (+2400000) (d)	Phase (d)	U (mag)	B (mag)	V (mag)	R (mag)	I (mag)	Telescope (Instrument)
55753.42	40.42	...	15.29 (0.01)	13.90 (0.02)	...	...	LT (RATCam)
55753.46	40.46	16.45 (0.05)	15.24 (0.01)	13.86 (0.01)	13.15 (0.01)	12.81 (0.01)	NOT (ALFOSC)
55755.40	42.40	16.42 (0.04)	15.30 (0.01)	13.96 (0.01)	13.23 (0.01)	12.89 (0.01)	NOT (ALFOSC)
55756.44	43.44	...	15.28 (0.02)	13.98 (0.02)	13.28 (0.02)	12.86 (0.01)	AS-Schmidt (SBIG)
55756.45	43.45	...	15.38 (0.02)	13.98 (0.01)	13.27 (0.03)	12.92 (0.01)	LT (RATCam)
55757.43	44.43	16.42 (0.04)	15.38 (0.01)	14.05 (0.01)	13.29 (0.01)	12.97 (0.01)	NOT (ALFOSC)
55759.45	46.45	...	15.44 (0.01)	14.06 (0.02)	...	...	LT (RATCam)
55761.40	48.40	...	15.44 (0.01)	14.17 (0.01)	13.44 (0.01)	13.02 (0.01)	AS-Schmidt (SBIG)
55762.41	49.41	...	15.45 (0.01)	14.16 (0.01)	13.44 (0.01)	13.06 (0.01)	NOT (ALFOSC)
55762.78	49.78	...	...	...	13.44 (0.01)	13.03 (0.01)	FTN (FS02)
55763.44	50.44	...	15.47 (0.01)	14.22 (0.01)	13.47 (0.01)	13.09 (0.01)	AS-Schmidt (SBIG)
55765.43	52.43	16.44 (0.03)	15.52 (0.01)	14.26 (0.01)	13.55 (0.01)	13.17 (0.01)	NOT (ALFOSC)
55767.43	54.43	16.50 (0.05)	...	...	13.58 (0.01)	13.16 (0.02)	LT (RATCam)
55768.45	55.45	16.48 (0.04)	...	...	13.60 (0.02)	13.19 (0.02)	LT (RATCam)
55771.40	58.40	16.37 (0.03)	15.58 (0.01)	14.32 (0.01)	13.62 (0.01)	13.28 (0.01)	CA-2.2m (CAFOS)
55773.39	60.39	16.45 (0.04)	15.60 (0.01)	14.38 (0.01)	13.71 (0.01)	13.32 (0.01)	NOT (ALFOSC)
55776.38	63.38	16.47 (0.04)	15.64 (0.01)	14.46 (0.01)	13.77 (0.01)	13.36 (0.01)	NOT (ALFOSC)
55777.33	64.33	...	15.52 (0.03)	14.46 (0.02)	13.78 (0.02)	13.34 (0.02)	AS-Schmidt (SBIG)
55780.40	67.40	16.42 (0.03)	15.65 (0.01)	14.50 (0.01)	13.85 (0.01)	13.43 (0.01)	NOT (ALFOSC)
55783.43	70.43	16.41 (0.03)	15.71 (0.01)	14.58 (0.01)	13.94 (0.01)	13.51 (0.01)	NOT (ALFOSC)
55784.33	71.33	...	15.66 (0.02)	14.59 (0.01)	...	13.43 (0.02)	AS-Schmidt (SBIG)
55784.39	71.39	16.45 (0.04)	15.66 (0.01)	14.52 (0.02)	13.90 (0.01)	13.47 (0.02)	CA-2.2m (CAFOS)
55784.77	71.77	...	...	...	13.93 (0.02)	13.45 (0.01)	FTN (FS02)
55785.36	72.36	...	15.70 (0.02)	14.61 (0.01)	13.96 (0.01)	13.45 (0.01)	AS-Schmidt (SBIG)
55788.41	75.41	...	...	...	14.02 (0.02)	13.52 (0.01)	AS-Schmidt (SBIG)
55790.38	77.38	16.45 (0.09)	...	...	14.03 (0.01)	13.61 (0.01)	LT (RATCam)
55793.37	80.37	16.55 (0.07)	15.80 (0.01)	14.74 (0.01)	14.13 (0.01)	13.67 (0.01)	NOT (ALFOSC)
55795.35	82.35	16.40 (0.04)	15.78 (0.01)	14.76 (0.01)	14.12 (0.01)	13.68 (0.01)	CA-2.2m (CAFOS)
55797.37	84.37	...	15.83 (0.02)	14.82 (0.01)	...	...	AS-Schmidt (SBIG)
55797.76	84.76	...	...	...	14.22 (0.01)	13.68 (0.01)	FTN (FS02)
55798.36	85.36	16.50 (0.03)	15.84 (0.01)	14.84 (0.01)	14.25 (0.01)	13.65 (0.02)	NOT (ALFOSC)
55799.33	86.33	...	15.82 (0.01)	14.86 (0.01)	...	...	AS-Schmidt (SBIG)
55801.36	88.36	16.44 (0.04)	15.89 (0.01)	14.90 (0.01)	14.31 (0.01)	13.80 (0.01)	NOT (ALFOSC)
55801.40	88.40	...	15.80 (0.02)	14.90 (0.01)	...	...	AS-Schmidt (SBIG)
55803.35	90.35	...	15.88 (0.02)	14.91 (0.01)	14.32 (0.01)	13.79 (0.01)	AS-Schmidt (SBIG)
55805.33	92.33	...	15.87 (0.02)	14.97 (0.02)	14.37 (0.01)	13.83 (0.01)	AS-Schmidt (SBIG)
55810.34	97.34	16.68 (0.06)	16.00 (0.01)	15.11 (0.01)	14.52 (0.01)	14.02 (0.01)	NOT (ALFOSC)
55812.33	99.33	16.51 (0.03)	16.02 (0.01)	15.05 (0.01)	14.49 (0.01)	14.00 (0.01)	CA-2.2m (CAFOS)
55817.35	104.35	...	16.02 (0.03)	15.19 (0.02)	14.63 (0.02)	14.04 (0.02)	AS-Schmidt (SBIG)
55818.33	105.33	...	16.10 (0.02)	15.19 (0.02)	14.66 (0.01)	14.08 (0.01)	AS-Schmidt (SBIG)
55821.31	108.31	16.77 (0.08)	16.12 (0.02)	15.25 (0.01)	14.68 (0.01)	14.16 (0.01)	CA-2.2m (CAFOS)
55824.32	111.32	...	...	15.31 (0.02)	14.75 (0.03)	14.24 (0.03)	AS-Schmidt (SBIG)
55827.33	114.33	...	16.16 (0.03)	15.42 (0.01)	14.87 (0.02)	14.27 (0.01)	AS-Schmidt (SBIG)
55827.48	114.48	...	16.22 (0.07)	15.37 (0.03)	14.94 (0.05)	14.38 (0.05)	AT (ANDOR)
55828.27	115.27	...	16.34 (0.04)	15.39 (0.02)	14.86 (0.02)	14.31 (0.01)	AT (ANDOR)
55830.28	117.28	...	16.30 (0.02)	15.38 (0.01)	14.91 (0.01)	14.34 (0.01)	AS-1.82m (AFOSC)
55834.26	121.26	...	16.23 (0.03)	15.49 (0.02)	14.99 (0.02)	14.44 (0.02)	AT (ANDOR)
55834.31	121.31	...	16.35 (0.02)	15.55 (0.01)	14.99 (0.02)	14.41 (0.02)	AS-Schmidt (SBIG)
55838.34	125.34	...	...	15.64 (0.02)	15.11 (0.03)	14.49 (0.01)	AS-Schmidt (SBIG)
55839.28	126.28	...	16.39 (0.03)	15.65 (0.02)	15.12 (0.02)	14.52 (0.02)	AS-Schmidt (SBIG)
55840.26	127.26	...	16.44 (0.03)	15.57 (0.02)	15.15 (0.03)	14.53 (0.02)	AT (ANDOR)
55840.30	127.30	...	16.44 (0.14)	15.93 (0.06)	15.08 (0.04)	14.59 (0.04)	AS-Schmidt (SBIG)

Table 4. Continued.

JD (+2400000) (d)	Phase (d)	U (mag)	B (mag)	V (mag)	R (mag)	I (mag)	Telescope (Instrument)
55846.26	133.26	...	16.60 (0.03)	15.77 (0.02)	15.17 (0.02)	14.71 (0.02)	AT (ANDOR)
55847.30	134.30	...	...	15.81 (0.02)	15.35 (0.03)	14.77 (0.02)	AT (ANDOR)
55849.26	136.26	...	16.68 (0.05)	15.81 (0.02)	15.33 (0.03)	14.75 (0.02)	AT (ANDOR)
55853.27	140.27	...	16.32 (0.06)	15.90 (0.05)	15.44 (0.05)	14.91 (0.04)	AS-Schmidt (SBIG)
55855.38	142.38	...	...	15.96 (0.03)	15.44 (0.03)	14.93 (0.03)	AT (ANDOR)
55856.24	143.24	...	16.72 (0.06)	16.01 (0.03)	15.42 (0.02)	14.91 (0.02)	AT (ANDOR)
55858.29	145.29	...	...	16.02 (0.03)	15.45 (0.03)	14.96 (0.02)	AT (ANDOR)
55859.23	146.23	...	16.84 (0.05)	16.08 (0.02)	15.56 (0.03)	15.01 (0.02)	AT (ANDOR)
55860.22	147.22	...	16.80 (0.05)	16.10 (0.03)	15.53 (0.03)	15.02 (0.02)	AT (ANDOR)
55864.69	151.69	17.55 (0.09)	16.94 (0.02)	16.14 (0.01)	15.65 (0.01)	15.10 (0.01)	AS-1.82m (AFOSC)
55866.28	153.28	...	...	16.23 (0.02)	15.64 (0.03)	15.18 (0.02)	AT (ANDOR)
55867.70	154.70	...	16.97 (0.02)	16.21 (0.03)	15.71 (0.02)	15.25 (0.02)	CA-2.2m (CAFOS)
55879.66	166.66	...	17.19 (0.03)	16.58 (0.02)	15.99 (0.02)	15.49 (0.02)	AS-Schmidt (SBIG)
55881.74	168.74	...	17.23 (0.02)	16.59 (0.02)	15.94 (0.01)	15.66 (0.03)	CA-2.2m (CAFOS)
55883.24	170.24	...	...	16.72 (0.05)	16.19 (0.05)	15.61 (0.02)	AT (ANDOR)
55885.21	172.21	...	17.67 (0.10)	16.53 (0.03)	15.98 (0.05)	15.62 (0.03)	AT (ANDOR)
55885.73	172.73	...	17.36 (0.08)	16.67 (0.02)	...	15.59 (0.03)	AS-1.82m (AFOSC)
55886.75	173.75	17.97 (0.03)	17.43 (0.01)	16.79 (0.01)	16.17 (0.01)	15.73 (0.01)	NOT (ALFOSC)
55893.71	180.71	...	...	16.93 (0.02)	16.27 (0.01)	15.80 (0.02)	AS-Schmidt (SBIG)
55894.76	181.76	18.12 (0.03)	17.58 (0.01)	16.96 (0.01)	16.31 (0.01)	15.89 (0.01)	NOT (ALFOSC)
55896.20	183.20	...	...	17.03 (0.05)	16.44 (0.06)	16.01 (0.04)	AT (ANDOR)
55898.19	185.19	...	17.44 (0.08)	17.06 (0.04)	16.35 (0.04)	15.90 (0.03)	AT (ANDOR)
55898.73	185.73	18.20 (0.04)	17.65 (0.01)	17.09 (0.01)	16.39 (0.01)	16.05 (0.01)	NOT (ALFOSC)
55903.76	190.76	18.11 (0.06)	17.74 (0.02)	17.18 (0.02)	16.48 (0.01)	16.10 (0.02)	NOT (ALFOSC)
55912.79	199.79	18.51 (0.05)	17.93 (0.02)	17.37 (0.01)	16.68 (0.01)	16.33 (0.01)	NOT (ALFOSC)
55922.76	209.76	18.70 (0.03)	18.10 (0.01)	17.57 (0.01)	16.86 (0.01)	16.52 (0.01)	NOT (ALFOSC)
55932.79	219.79	18.77 (0.06)	18.26 (0.01)	17.80 (0.02)	16.97 (0.02)	16.72 (0.02)	NOT (ALFOSC)
55939.73	226.73	18.93 (0.05)	18.40 (0.02)	17.92 (0.02)	17.12 (0.01)	16.85 (0.01)	NOT (ALFOSC)
55948.73	235.73	19.11 (0.04)	18.56 (0.01)	18.08 (0.01)	17.27 (0.01)	17.04 (0.01)	NOT (ALFOSC)
55955.76	242.76	19.23 (0.04)	18.69 (0.01)	18.20 (0.01)	17.37 (0.01)	17.19 (0.01)	NOT (ALFOSC)
55975.69	262.69	19.61 (0.05)	19.01 (0.01)	18.59 (0.01)	17.67 (0.01)	17.51 (0.01)	NOT (ALFOSC)
55982.74	269.74	19.88 (0.07)	19.09 (0.02)	18.69 (0.02)	17.74 (0.01)	17.65 (0.01)	NOT (ALFOSC)
55986.62	273.62	19.88 (0.11)	19.15 (0.03)	18.75 (0.03)	17.76 (0.02)	17.83 (0.03)	CA-2.2m (CAFOS)
55987.62	274.62	19.59 (0.12)	19.11 (0.02)	18.76 (0.02)	17.78 (0.01)	17.78 (0.01)	LT (RATCam)
55998.67	285.67	...	19.43 (0.02)	18.96 (0.02)	18.00 (0.01)	17.95 (0.01)	NOT (ALFOSC)
56008.66	295.66	...	19.40 (0.03)	19.10 (0.03)	18.06 (0.02)	18.14 (0.03)	LT (RATCam)
56014.51	301.51	20.28 (0.07)	19.65 (0.01)	19.24 (0.02)	18.26 (0.01)	18.22 (0.01)	NOT (ALFOSC)
56026.49	313.49	...	19.86 (0.02)	19.44 (0.02)	18.47 (0.01)	18.41 (0.02)	NOT (ALFOSC)
56043.59	330.59	20.76 (0.06)	20.15 (0.02)	19.78 (0.02)	18.72 (0.01)	18.72 (0.02)	NOT (ALFOSC)
56071.42	358.42	...	20.61 (0.02)	20.28 (0.04)	19.20 (0.02)	19.36 (0.03)	NOT (ALFOSC)
56087.43	374.43	...	20.86 (0.02)	20.48 (0.03)	19.45 (0.02)	19.62 (0.02)	NOT (ALFOSC)
56096.48	383.48	21.62 (0.10)	20.95 (0.03)	20.60 (0.04)	19.51 (0.02)	19.81 (0.03)	NOT (ALFOSC)
56115.44	402.44	...	21.26 (0.03)	20.96 (0.05)	19.91 (0.02)	20.18 (0.04)	NOT (ALFOSC)
56132.43	419.43	...	21.38 (0.06)	21.07 (0.06)	20.19 (0.03)	20.49 (0.05)	NOT (ALFOSC)
56133.40	420.40	...	21.55 (0.05)	21.13 (0.06)	20.19 (0.03)	...	NOT (ALFOSC)
56154.39	441.39	...	21.76 (0.05)	21.46 (0.06)	20.58 (0.04)	21.01 (0.08)	NOT (ALFOSC)
56180.37	467.37	...	22.30 (0.05)	21.82 (0.06)	20.90 (0.04)	...	NOT (ALFOSC)
56313.73	600.73	...	...	22.44 (0.10)	...	...	NOT (ALFOSC)
56353.50	640.50	...	...	23.02 (0.00)	...	22.58 (0.00)	HST (ACS)
56371.69	658.69	...	23.42 (0.32)	...	...	...	NOT (ALFOSC)
56397.64	684.64	...	...	23.20 (0.20)	...	...	NOT (ALFOSC)
56445.43	732.43	...	23.96 (0.50)	...	...	...	NOT (ALFOSC)

Table 5. Optical colour-corrected SDSS *u* and S-corrected SDSS *griz* magnitudes for SN 2011dh. Errors are given in parentheses. For completeness data for the first 100 days already published in E14a are included.

JD (+2400000) (d)	Phase (d)	*u* (mag)	*g* (mag)	*r* (mag)	*i* (mag)	*z* (mag)	Telescope (Instrument)
55716.47	3.47	15.90 (0.03)	15.08 (0.01)	14.68 (0.01)	14.80 (0.01)	14.76 (0.02)	LT (RATCam)
55717.46	4.46	16.01 (0.03)	14.80 (0.01)	14.38 (0.01)	14.61 (0.01)	14.58 (0.02)	LT (RATCam)
55718.53	5.53	...	14.44 (0.04)	14.06 (0.01)	14.27 (0.01)	...	LT (RATCam)
55720.44	7.44	15.39 (0.02)	13.97 (0.01)	13.53 (0.01)	13.73 (0.02)	13.87 (0.01)	LT (RATCam)
55721.44	8.44	15.09 (0.01)	13.78 (0.01)	13.33 (0.01)	13.52 (0.01)	13.64 (0.01)	LT (RATCam)
55722.44	9.44	...	13.59 (0.01)	13.18 (0.01)	13.35 (0.01)	13.49 (0.01)	LT (RATCam)
55723.41	10.41	14.82 (0.03)	...	13.02 (0.01)	13.16 (0.01)	13.34 (0.01)	LT (RATCam)
55724.41	11.41	14.72 (0.02)	...	12.93 (0.01)	13.05 (0.01)	13.22 (0.01)	LT (RATCam)
55725.43	12.43	14.74 (0.04)	...	12.83 (0.01)	12.94 (0.01)	13.09 (0.01)	LT (RATCam)
55729.39	16.39	14.56 (0.03)	13.10 (0.01)	12.56 (0.01)	12.62 (0.01)	12.81 (0.01)	LT (RATCam)
55730.40	17.40	14.45 (0.03)	13.07 (0.01)	12.51 (0.01)	12.56 (0.01)	12.77 (0.01)	LT (RATCam)
55731.41	18.41	14.54 (0.03)	13.02 (0.01)	12.46 (0.01)	12.51 (0.01)	12.71 (0.01)	LT (RATCam)
55731.82	18.82	...	13.07 (0.01)	12.46 (0.01)	12.50 (0.01)	12.65 (0.01)	FTN (FS02)
55732.46	19.46	14.56 (0.01)	13.00 (0.03)	12.42 (0.01)	12.48 (0.01)	12.67 (0.01)	LT (RATCam)
55733.45	20.45	14.52 (0.05)	13.03 (0.01)	12.41 (0.01)	12.45 (0.01)	12.65 (0.01)	LT (RATCam)
55735.44	22.44	14.75 (0.04)	13.12 (0.01)	12.43 (0.01)	12.41 (0.01)	12.60 (0.01)	LT (RATCam)
55736.44	23.44	14.96 (0.03)	13.19 (0.02)	12.45 (0.01)	12.42 (0.01)	12.59 (0.02)	LT (RATCam)
55738.45	25.45	15.37 (0.02)	13.43 (0.01)	12.55 (0.01)	12.47 (0.01)	12.65 (0.01)	LT (RATCam)
55739.44	26.44	15.55 (0.02)	13.50 (0.03)	12.59 (0.01)	12.50 (0.01)	12.65 (0.01)	LT (RATCam)
55740.44	27.44	15.80 (0.01)	13.66 (0.01)	12.66 (0.01)	12.55 (0.01)	12.70 (0.01)	LT (RATCam)
55741.44	28.44	...	13.75 (0.02)	12.76 (0.01)	12.59 (0.02)	12.76 (0.01)	LT (RATCam)
55742.49	29.49	16.20 (0.02)	13.92 (0.01)	12.84 (0.01)	12.65 (0.01)	12.80 (0.01)	LT (RATCam)
55745.44	32.44	16.71 (0.05)	14.20 (0.02)	13.04 (0.01)	12.79 (0.01)	12.87 (0.03)	LT (RATCam)
55745.80	32.80	...	14.35 (0.04)	13.00 (0.01)	12.79 (0.01)	12.94 (0.01)	FTN (FS02)
55746.45	33.45	16.83 (0.04)	14.32 (0.01)	13.09 (0.01)	12.82 (0.01)	12.94 (0.01)	LT (RATCam)
55747.44	34.44	16.90 (0.04)	14.40 (0.02)	13.13 (0.01)	12.86 (0.01)	12.95 (0.01)	LT (RATCam)
55748.44	35.44	17.09 (0.04)	14.42 (0.02)	13.19 (0.01)	12.90 (0.01)	13.01 (0.01)	LT (RATCam)
55750.44	37.44	17.20 (0.10)	14.55 (0.02)	13.29 (0.01)	13.02 (0.02)	13.04 (0.04)	LT (RATCam)
55751.43	38.43	17.14 (0.03)	14.64 (0.03)	13.36 (0.01)	13.04 (0.01)	13.11 (0.01)	LT (RATCam)
55752.45	39.45	17.24 (0.07)	14.66 (0.01)	13.39 (0.01)	13.04 (0.01)	13.09 (0.01)	LT (RATCam)
55756.46	43.46	...	14.79 (0.01)	13.55 (0.01)	13.22 (0.01)	13.19 (0.01)	LT (RATCam)
55762.78	49.78	...	15.00 (0.02)	13.68 (0.01)	13.37 (0.01)	13.28 (0.01)	FTN (FS02)
55767.43	54.43	17.30 (0.02)	15.03 (0.01)	13.84 (0.01)	13.52 (0.01)	13.38 (0.02)	LT (RATCam)
55768.45	55.45	17.29 (0.02)	15.03 (0.01)	13.86 (0.01)	13.56 (0.01)	13.41 (0.01)	LT (RATCam)
55773.39	60.39	17.27 (0.04)	15.07 (0.01)	13.99 (0.01)	13.72 (0.01)	13.54 (0.02)	NOT (ALFOSC)
55776.38	63.38	17.36 (0.03)	15.13 (0.01)	14.03 (0.01)	13.76 (0.01)	13.56 (0.01)	NOT (ALFOSC)
55780.41	67.41	17.33 (0.03)	15.16 (0.01)	14.09 (0.01)	13.84 (0.01)	13.61 (0.01)	NOT (ALFOSC)
55783.44	70.44	17.26 (0.04)	15.18 (0.01)	14.19 (0.01)	13.93 (0.01)	13.67 (0.01)	NOT (ALFOSC)
55784.77	71.77	...	15.23 (0.02)	14.16 (0.01)	13.88 (0.01)	13.64 (0.01)	FTN (FS02)
55790.38	77.38	17.29 (0.03)	15.35 (0.04)	14.28 (0.01)	14.04 (0.01)	13.69 (0.02)	LT (RATCam)
55793.37	80.37	17.32 (0.03)	15.30 (0.01)	14.39 (0.01)	14.16 (0.01)	13.84 (0.01)	NOT (ALFOSC)
55797.76	84.76	...	15.38 (0.01)	14.42 (0.01)	14.18 (0.01)	13.82 (0.01)	FTN (FS02)
55798.37	85.37	17.35 (0.03)	15.38 (0.01)	14.50 (0.01)	14.26 (0.01)	13.87 (0.01)	NOT (ALFOSC)
55801.36	88.36	17.34 (0.01)	15.42 (0.01)	14.53 (0.01)	14.31 (0.01)	13.89 (0.01)	NOT (ALFOSC)
55810.34	97.34	17.49 (0.02)	15.55 (0.01)	14.75 (0.01)	14.56 (0.01)	14.10 (0.02)	NOT (ALFOSC)
55886.75	173.75	21.74 (1.97)	16.99 (0.01)	16.36 (0.01)	16.16 (0.01)	...	NOT (ALFOSC)
55894.76	181.76	18.89 (0.03)	17.19 (0.02)	16.50 (0.01)	16.28 (0.02)	16.31 (0.02)	NOT (ALFOSC)
55898.73	185.73	18.97 (0.03)	17.25 (0.01)	16.59 (0.01)	16.42 (0.01)	16.49 (0.01)	NOT (ALFOSC)
55903.76	190.76	19.07 (0.05)	17.32 (0.02)	16.68 (0.01)	16.47 (0.01)	16.68 (0.04)	NOT (ALFOSC)
55912.79	199.79	19.28 (0.04)	17.48 (0.02)	16.86 (0.01)	16.66 (0.01)	16.79 (0.03)	NOT (ALFOSC)

Table 5. Continued.

JD (+2400000) (d)	Phase (d)	*u* (mag)	*g* (mag)	*r* (mag)	*i* (mag)	*z* (mag)	Telescope (Instrument)
55922.77	209.77	19.44 (0.02)	17.71 (0.01)	17.05 (0.01)	16.83 (0.01)	17.18 (0.01)	NOT (ALFOSC)
55932.79	219.79	19.50 (0.05)	17.83 (0.02)	17.18 (0.02)	17.01 (0.02)	17.37 (0.04)	NOT (ALFOSC)
55939.74	226.74	19.74 (0.05)	18.02 (0.01)	17.31 (0.01)	17.11 (0.01)	17.49 (0.02)	NOT (ALFOSC)
55948.73	235.73	19.87 (0.03)	18.15 (0.01)	17.45 (0.01)	17.27 (0.01)	17.74 (0.01)	NOT (ALFOSC)
55955.76	242.76	20.01 (0.03)	18.27 (0.01)	17.57 (0.01)	17.40 (0.01)	17.87 (0.02)	NOT (ALFOSC)
55975.69	262.69	20.37 (0.04)	18.64 (0.01)	17.84 (0.01)	17.71 (0.01)	18.25 (0.02)	NOT (ALFOSC)
55982.74	269.74	20.64 (0.05)	18.74 (0.01)	17.92 (0.01)	17.86 (0.01)	18.42 (0.03)	NOT (ALFOSC)
55987.62	274.62	20.47 (0.11)	18.76 (0.01)	17.95 (0.01)	17.96 (0.01)	18.30 (0.03)	LT (RATCam)
56008.66	295.66	...	19.14 (0.02)	18.22 (0.01)	18.33 (0.03)	19.27 (0.10)	LT (RATCam)
56014.52	301.52	21.28 (0.04)	19.30 (0.01)	18.40 (0.01)	18.45 (0.01)	19.02 (0.02)	NOT (ALFOSC)
56043.60	330.60	21.73 (0.03)	19.82 (0.01)	18.82 (0.01)	18.96 (0.01)	19.52 (0.03)	NOT (ALFOSC)
56071.43	358.43	21.85 (0.06)	20.27 (0.02)	19.26 (0.02)	19.62 (0.03)	19.98 (0.05)	NOT (ALFOSC)
56096.49	383.49	22.35 (0.05)	20.61 (0.02)	19.55 (0.02)	20.09 (0.03)	...	NOT (ALFOSC)
56132.43	419.43	...	21.14 (0.03)	20.21 (0.03)	20.79 (0.05)	21.25 (0.17)	NOT (ALFOSC)
56133.41	420.41	...	21.30 (0.04)	20.21 (0.03)	20.95 (0.06)	...	NOT (ALFOSC)
56154.39	441.39	...	21.50 (0.04)	20.61 (0.03)	21.32 (0.07)	...	NOT (ALFOSC)
56313.75	600.75	...	...	22.46 (0.11)	...	...	NOT (ALFOSC)
56428.46	715.46	...	...	23.10 (0.20)	...	...	NOT (ALFOSC)

Table 6. NIR S-corrected 2MASS *JHK* magnitudes for SN 2011dh. Errors are given in parentheses. For completeness data for the first 100 days already published in E14a are included.

JD (+2400000) (d)	Phase (d)	*J* (mag)	*H* (mag)	*K* (mag)	Telescope (Instrument)
55716.51	3.51	14.09 (0.01)	13.90 (0.01)	13.68 (0.02)	TNG (NICS)
55722.40	9.40	12.89 (0.01)	12.87 (0.01)	12.67 (0.01)	TNG (NICS)
55725.50	12.50	12.61 (0.04)	12.54 (0.01)	12.43 (0.02)	NOT (NOTCAM)
55730.51	17.51	12.12 (0.01)	12.08 (0.01)	11.94 (0.01)	TNG (NICS)
55737.72	24.72	11.96 (0.01)	11.90 (0.01)	11.72 (0.03)	LBT (LUCIFER)
55741.13	28.13	11.94 (0.01)	11.90 (0.02)	11.70 (0.05)	TCS (CAIN)
55748.43	35.43	12.14 (0.01)	12.00 (0.02)	11.77 (0.01)	TCS (CAIN)
55750.42	37.42	12.19 (0.01)	12.00 (0.01)	11.84 (0.04)	TCS (CAIN)
55751.42	38.42	12.29 (0.01)	12.01 (0.01)	11.84 (0.03)	TCS (CAIN)
55758.45	45.45	12.55 (0.01)	12.22 (0.01)	12.06 (0.01)	TNG (NICS)
55759.41	46.41	12.49 (0.03)	12.22 (0.03)	12.11 (0.04)	TCS (CAIN)
55762.41	49.41	12.57 (0.01)	12.26 (0.01)	12.17 (0.03)	TCS (CAIN)
55763.42	50.42	12.62 (0.02)	12.27 (0.04)	12.25 (0.06)	TCS (CAIN)
55765.45	52.45	12.79 (0.01)	12.38 (0.01)	12.23 (0.01)	TNG (NICS)
55769.41	56.41	12.77 (0.01)	12.48 (0.06)	12.40 (0.03)	TCS (CAIN)
55773.37	60.37	12.94 (0.03)	12.58 (0.01)	12.42 (0.02)	TNG (NICS)
55774.40	61.40	12.90 (0.01)	12.55 (0.03)	12.43 (0.04)	TCS (CAIN)
55776.40	63.40	13.00 (0.01)	12.64 (0.01)	12.53 (0.02)	TCS (CAIN)
55781.41	68.41	13.23 (0.01)	12.76 (0.01)	12.66 (0.01)	WHT (LIRIS)
55787.44	74.44	13.56 (0.03)	13.03 (0.02)	12.95 (0.02)	NOT (NOTCAM)
55801.36	88.36	13.90 (0.02)	13.41 (0.02)	13.17 (0.01)	TNG (NICS)
55804.34	91.34	14.10 (0.01)	13.50 (0.01)	13.26 (0.01)	CA-3.5m (O2000)
55814.32	101.32	14.38 (0.01)	13.80 (0.01)	13.50 (0.01)	CA-3.5m (O2000)
55818.36	105.36	14.45 (0.02)	13.91 (0.01)	13.74 (0.01)	NOT (NOTCAM)
55880.72	167.72	16.23 (0.01)	15.38 (0.01)	14.70 (0.01)	CA-3.5m (O2000)
55913.68	200.68	17.00 (0.01)	16.19 (0.02)	15.31 (0.02)	CA-3.5m (O2000)
55914.66	201.66	17.05 (0.01)	16.23 (0.02)	15.35 (0.02)	CA-3.5m (O2000)
55946.13	233.13	17.43 (0.02)	16.78 (0.02)	16.21 (0.02)	UKIRT (WFCAM)
55999.91	286.91	18.10 (0.02)	17.47 (0.02)	17.31 (0.02)	UKIRT (WFCAM)
56024.38	311.38	18.46 (0.03)	17.80 (0.03)	17.71 (0.04)	WHT (LIRIS)
56052.47	339.47	18.69 (0.02)	17.96 (0.02)	18.60 (0.03)	WHT (LIRIS)
56093.48	380.48	19.71 (0.06)	18.71 (0.06)	19.21 (0.08)	WHT (LIRIS)

Table 7. MIR Spitzer 3.6 μm and 4.5 μm magnitudes for SN 2011dh. Errors are given in parentheses. For completeness data for the first 100 days already published in E14a are included.

JD (+2400000) (d)	Phase (d)	3.6 μm (mag)	4.5 μm (mag)	Telescope (Instrument)
55731.21	18.21	11.83 (0.02)	11.48 (0.02)	SPITZER (IRAC)
55737.06	24.06	11.66 (0.02)	11.31 (0.02)	SPITZER (IRAC)
55744.32	31.32	11.66 (0.02)	11.30 (0.02)	SPITZER (IRAC)
55751.46	38.46	11.68 (0.02)	11.30 (0.02)	SPITZER (IRAC)
55758.75	45.75	11.79 (0.02)	11.32 (0.02)	SPITZER (IRAC)
55766.45	53.45	11.96 (0.02)	11.34 (0.02)	SPITZER (IRAC)
55772.33	59.33	12.11 (0.03)	11.38 (0.02)	SPITZER (IRAC)
55779.12	66.12	12.30 (0.03)	11.43 (0.02)	SPITZER (IRAC)
55785.60	72.60	12.50 (0.03)	11.50 (0.02)	SPITZER (IRAC)
55798.28	85.28	12.84 (0.04)	11.66 (0.03)	SPITZER (IRAC)
55964.14	251.14	14.34 (0.09)	13.31 (0.07)	SPITZER (IRAC)
56026.63	313.63	15.57 (0.15)	14.27 (0.11)	SPITZER (IRAC)
56104.23	391.23	17.12 (0.32)	15.54 (0.19)	SPITZER (IRAC)
56136.41	423.41	17.46 (0.37)	16.01 (0.24)	SPITZER (IRAC)
56168.69	455.69	17.63 (0.40)	16.25 (0.26)	SPITZER (IRAC)
56337.59	624.59	18.42 (0.57)	17.59 (0.49)	SPITZER (IRAC)

Table 8. List of late-time (100-415 days) optical and NIR spectroscopic observations.

JD (+2400000) (d)	Phase (d)	Grism	Range (Å)	Resolution	Resolution (Å)	Telescope (Instrument)
55821.33	108.33	b200	3300-8700	...	12.0	CA-2.2m (CAFOS)
55821.33	108.33	r200	6300-10500	...	12.0	CA-2.2m (CAFOS)
55828.35	115.35	R300B	3200-5300	...	4.1	WHT (ISIS)
55828.35	115.35	R158R	5300-10000	...	7.7	WHT (ISIS)
55830.25	117.25	Grism 4	3500-8450	613	...	AS 1.82m (AFOSC)
55864.65	151.65	Grism 4	3500-8450	613	...	AS 1.82m (AFOSC)
55867.71	154.71	?	?-?	...	?	CA-2.2m (CAFOS)
55893.76	180.76	Grism 3	3200-6700	345	12.4	NOT (ALFOSC)
55897.76	184.76	Grism 5	5000-10250	415	16.8	NOT (ALFOSC)
55911.20	198.20	zJ	8900-15100	700	...	WHT (LIRIS)
55914.70	201.70	R300B	3200-5300	...	8.2	WHT (ISIS)
55914.70	201.70	R158R	5300-10000	...	15.4	WHT (ISIS)
55918.69	205.69	HK	14000-25000	333	...	TNG (NICS)
55951.64	238.64	Grism 4	3200-9100	355	16.2	NOT (ALFOSC)
55998.68	285.68	r200	6300-10500	...	12.0	CA-2.2m (CAFOS)
56005.63	292.63	Grism 4	3200-9100	355	16.2	NOT (ALFOSC)
56013.14	300.14	R600B	?-?	...	5.7	WHT (ISIS)
56013.14	300.14	R316R	?-?	...	3.0	WHT (ISIS)
56071.56	358.56	R500B	3440-7600	322	15.0	GTC (OSIRIS)
56072.61	359.61	R500R	4800-10000	352	20.8	GTC (OSIRIS)
56128.47	415.47	R300B	3600-7000	270	16.7	GTC (OSIRIS)

Table 9. Pseudo-bolometric 3-300 days UV to MIR lightcurve for SN 2011dh calculated from spectroscopic and photometric data with a 1-day sampling between 3 and 50 days and a 5-day sampling between 50 and 300 days. Random errors are given in the first parentheses and systematic lower and upper errors (arising from the distance and extinction) respectively in the second parentheses.

JD (+2400000) (d)	Phase (d)	L (log erg s^{-1})	JD (+2400000) (d)	Phase (d)	L (log erg s^{-1})
55717.00	4.00	41.465 (0.001) (0.098,0.186)	55773.00	60.00	41.670 (0.002) (0.093,0.160)
55718.00	5.00	41.553 (0.001) (0.097,0.181)	55778.00	65.00	41.627 (0.002) (0.093,0.160)
55719.00	6.00	41.653 (0.001) (0.097,0.179)	55783.00	70.00	41.585 (0.002) (0.093,0.161)
55720.00	7.00	41.747 (0.001) (0.097,0.178)	55788.00	75.00	41.544 (0.002) (0.093,0.161)
55721.00	8.00	41.835 (0.001) (0.097,0.178)	55793.00	80.00	41.502 (0.002) (0.093,0.161)
55722.00	9.00	41.909 (0.001) (0.097,0.178)	55798.00	85.00	41.460 (0.002) (0.093,0.162)
55723.00	10.00	41.970 (0.001) (0.097,0.177)	55803.00	90.00	41.417 (0.002) (0.094,0.162)
55724.00	11.00	42.019 (0.001) (0.097,0.176)	55808.00	95.00	41.375 (0.002) (0.094,0.163)
55725.00	12.00	42.057 (0.001) (0.097,0.176)	55813.00	100.00	41.333 (0.002) (0.094,0.163)
55726.00	13.00	42.089 (0.001) (0.096,0.175)	55818.00	105.00	41.291 (0.002) (0.094,0.163)
55727.00	14.00	42.118 (0.001) (0.096,0.174)	55823.00	110.00	41.249 (0.001) (0.094,0.164)
55728.00	15.00	42.142 (0.001) (0.096,0.174)	55828.00	115.00	41.208 (0.001) (0.094,0.164)
55729.00	16.00	42.164 (0.001) (0.096,0.173)	55833.00	120.00	41.166 (0.001) (0.094,0.164)
55730.00	17.00	42.182 (0.001) (0.096,0.173)	55838.00	125.00	41.124 (0.001) (0.094,0.164)
55731.00	18.00	42.198 (0.001) (0.096,0.173)	55843.00	130.00	41.081 (0.002) (0.094,0.164)
55732.00	19.00	42.209 (0.001) (0.096,0.172)	55848.00	135.00	41.038 (0.002) (0.094,0.165)
55733.00	20.00	42.214 (0.001) (0.096,0.172)	55853.00	140.00	40.995 (0.001) (0.094,0.165)
55734.00	21.00	42.216 (0.001) (0.096,0.171)	55858.00	145.00	40.953 (0.001) (0.094,0.165)
55735.00	22.00	42.211 (0.001) (0.095,0.171)	55863.00	150.00	40.909 (0.001) (0.094,0.165)
55736.00	23.00	42.201 (0.001) (0.095,0.170)	55868.00	155.00	40.863 (0.001) (0.094,0.165)
55737.00	24.00	42.186 (0.001) (0.095,0.169)	55873.00	160.00	40.817 (0.001) (0.094,0.165)
55738.00	25.00	42.165 (0.001) (0.095,0.167)	55878.00	165.00	40.772 (0.001) (0.094,0.165)
55739.00	26.00	42.142 (0.001) (0.094,0.166)	55883.00	170.00	40.726 (0.001) (0.094,0.164)
55740.00	27.00	42.117 (0.001) (0.094,0.165)	55888.00	175.00	40.681 (0.001) (0.094,0.164)
55741.00	28.00	42.091 (0.001) (0.094,0.164)	55893.00	180.00	40.637 (0.001) (0.094,0.164)
55742.00	29.00	42.064 (0.001) (0.094,0.163)	55898.00	185.00	40.594 (0.001) (0.094,0.164)
55743.00	30.00	42.039 (0.001) (0.094,0.162)	55903.00	190.00	40.552 (0.001) (0.094,0.164)
55744.00	31.00	42.016 (0.001) (0.093,0.162)	55908.00	195.00	40.512 (0.001) (0.094,0.164)
55745.00	32.00	41.996 (0.001) (0.093,0.161)	55913.00	200.00	40.472 (0.001) (0.094,0.164)
55746.00	33.00	41.977 (0.001) (0.093,0.161)	55918.00	205.00	40.432 (0.001) (0.094,0.164)
55747.00	34.00	41.959 (0.001) (0.093,0.160)	55923.00	210.00	40.396 (0.001) (0.094,0.164)
55748.00	35.00	41.943 (0.001) (0.093,0.160)	55928.00	215.00	40.362 (0.001) (0.094,0.164)
55749.00	36.00	41.928 (0.001) (0.093,0.160)	55933.00	220.00	40.327 (0.001) (0.094,0.164)
55750.00	37.00	41.914 (0.001) (0.093,0.159)	55938.00	225.00	40.294 (0.001) (0.094,0.164)
55751.00	38.00	41.900 (0.001) (0.093,0.159)	55943.00	230.00	40.262 (0.001) (0.094,0.164)
55752.00	39.00	41.887 (0.001) (0.093,0.159)	55948.00	235.00	40.230 (0.001) (0.094,0.164)
55753.00	40.00	41.874 (0.001) (0.093,0.159)	55953.00	240.00	40.200 (0.001) (0.094,0.163)
55754.00	41.00	41.861 (0.001) (0.093,0.159)	55958.00	245.00	40.169 (0.001) (0.094,0.163)
55755.00	42.00	41.848 (0.001) (0.093,0.159)	55963.00	250.00	40.137 (0.001) (0.094,0.163)
55756.00	43.00	41.836 (0.001) (0.093,0.159)	55968.00	255.00	40.104 (0.001) (0.094,0.163)
55757.00	44.00	41.823 (0.001) (0.093,0.159)	55973.00	260.00	40.071 (0.001) (0.094,0.163)
55758.00	45.00	41.812 (0.001) (0.093,0.159)	55978.00	265.00	40.039 (0.001) (0.094,0.163)
55759.00	46.00	41.802 (0.001) (0.093,0.159)	55983.00	270.00	40.006 (0.001) (0.094,0.163)
55760.00	47.00	41.792 (0.001) (0.093,0.159)	55988.00	275.00	39.973 (0.001) (0.094,0.163)
55761.00	48.00	41.782 (0.001) (0.093,0.159)	55993.00	280.00	39.940 (0.001) (0.094,0.163)
55762.00	49.00	41.773 (0.002) (0.093,0.159)	55998.00	285.00	39.907 (0.001) (0.094,0.163)
55763.00	50.00	41.763 (0.002) (0.093,0.159)	56003.00	290.00	39.873 (0.001) (0.094,0.163)
55768.00	55.00	41.716 (0.002) (0.093,0.159)	56008.00	295.00	39.838 (0.001) (0.094,0.163)